

# Multivariate Approach Reveals a Higher Likelihood of Compound Heat Stress-Pluvial Floods in Urban India

Poulomi Ganguli<sup>1</sup> and Sucheta Pradhan<sup>1</sup>

<sup>1</sup>Indian Institute of Technology Kharagpur

November 22, 2022

## Abstract

The cascade hazard, heat stress (preconditioned) and heavy rainfall (response) in close succession have become frequent in several areas of the globe, causing critical infrastructure failures. Although some regions of South Asia witness deadly humid heat stress, little is known about the linkage of humid heat stress (*HHS*; high temperature compounded by humidity) versus record rainfall and cascade hazard due to compound (same or lagged-day) occurrences of both extremes. We leverage ground-based meteorological records from 1970-2018 to analyze the risk of extreme precipitation preceded by heat stress over selected urban locations of India using a multivariate conditional-probability approach. We show that humid heat is *likely* to intensify the extreme rainfall, especially during the core monsoon (June-September) season. This phenomenon is associated with moisture convergence and large upper tail distributions of peak precipitation over several sites. Our insights to compound flood hazard would benefit (re)-insurance and flash flood forecast, devising adaptations.

## Hosted file

essoar.10510858.1.docx available at <https://authorea.com/users/537726/articles/599412-multivariate-approach-reveals-a-higher-likelihood-of-compound-heat-stress-pluvial-floods-in-urban-india>

Poulomi Ganguli<sup>1</sup>, Sucheta Pradhan<sup>1</sup>

<sup>1</sup>Agricultural and Food Engineering Department, Indian Institute of Technology Kharagpur, Kharagpur, India.

Corresponding author: P. Ganguli (pganguli@agfe.iitkgp.ac.in)

Key Points:

- We propose a conditional probability-based approach to attribute severity of precipitation extremes considering heat stress as covariate.
- Extreme precipitation preceded by humid heat stress tend to show larger frequency during southwest monsoon season.
- Cities near the coast tend to reach 'real' tipping points indicating larger risk of cascade hazard owing to heat stress-rainfall extremes.

Abstract

The cascade hazard, heat stress (preconditioned) and heavy rainfall (response) in close succession have become frequent in several areas of the globe, causing critical infrastructure failures. Although some regions of South Asia witness deadly humid heat stress, little is known about the linkage of humid heat stress (*HHS*; high temperature compounded by humidity) versus record rainfall and cascade hazard due to compound (same or lagged-day) occurrences of both extremes. We leverage ground-based meteorological records from 1970-2018 to analyze the risk of extreme precipitation preceded by heat stress over selected urban locations of India using a multivariate conditional-probability approach. We show that humid heat is *likely* to intensify the extreme rainfall, especially during the core monsoon (June-September) season. This phenomenon is associated with moisture convergence and large upper tail distributions of peak precipitation over several sites. Our insights to compound flood hazard would benefit (re)-insurance and flash flood forecast, devising adaptations.

### Plain Language Summary

This study contributes to an understanding of multivariate (same time and place) and sequential (preconditioned, i.e., multiple times and same place) compound extremes, humid heat stress and heavy rainfall, impacting the system vulnerability. Although several studies assessed the likelihood of compound heat-moisture stresses and its impact, very few have explored humid heat stress-precipitation couplings in driving concurrent heat-pluvial floods. Typically, climate-informed extreme rainfall assessments in South Asia and elsewhere rely on covariate-based extreme value analysis considering air temperature (i.e., sensible heat flux), as an influencing driver. We propose a conditional probability-based approach to identify the severity of extreme precipitation, considering humid heat stress as a compounding driver. We demonstrate the potentials of the model using ground-based observations over notable urban and peri-urban localities of India, representing seven homogeneous (rainfall) climatic zones of the country. Our analysis reveals that considering the upper limit of human

survivability (i.e., wet bulb temperature  $> 32^{\circ}\text{C}$ ), the western half of the country showed a robust amplification in extreme precipitation. Further, coastal cities tend to attain or exceed the wet-bulb temperature threshold, indicating a larger risk of cascade hazard (i.e., heat stress and heavy rainfall in close succession), triggering critical infrastructure failures and widespread urban flooding.

## 1 Introduction

Climate change is expected to alter the frequency and intensity of rare extreme events, such as heat stress, flooding, and the compound interactions between such unprecedented extremes (Masson-Delmotte et al., 2021). Several regions of South Asia have witnessed deadly heatwaves in recent decades in densely inhabited localities (Im et al., 2017; Saeed et al., 2021), threatening the sustainability of rapidly growing urban settlements. Exposure to dangerously high temperatures endangers the health and development of cities, resulting in reductions in labour productivity and economic output (Fechter-Leggett et al., 2016; Dasgupta et al., 2021). Extreme precipitation and flooding pose considerable risks, impacting more than 70 million population globally each year, estimated in 2018 (CRED, 2018). The frequency and intensity of extreme rainfall have increased over several areas of India over the past few decades (Krishnamurthy et al., 2009). Furthermore, a potential link between human contribution to heat waves and heavy precipitation has been shown earlier (Fischer & Knutti, 2015).

Humidity plays a vital role in intensifying heat stress because the hot and humid environment affects thermal comfort level as it is difficult to remove heat via evaporation (Davis et al., 2016). Few studies have shown an upward trend in heatwaves and its relationship to dry spells over India (Rohini et al., 2016; Sharma & Mujumdar, 2017). Nevertheless, the focus has been on the sensible heat content of air, solely considering ‘dry-bulb’ temperature (i.e., air temperature) or emphasizing causal relationships of dry-bulb temperature versus extreme precipitation (Agilan & Umamahesh, 2017; Risser & Wehner, 2017).

We hypothesize that HHS will potentially augment convective available potential energy (CAPE), leading to severe storm events and frequent flooding. In this paper, we analyze the hazard cascade over selected urban locations of India (Figure 1a-b) with a copula-based conditional probability (CCP; Figure 1c) framework (Nelsen, 2013). While HHS can potentially collapse critical infrastructures, such as electrical power grid failure (Stone Jr et al., 2021), the concurrence of extreme precipitation within a short time window would collapse the urban-storm water drainage systems (Rosenzweig et al., 2018). Inferences are based on high-quality meteorological observations during the past five decades (1970-2018) over densely populated nine urban locations (Table S1) of India. We define two types of compound events, *Case I*: Peak over threshold (POT) wet bulb temperature coincide/precedes by POT extreme precipitation event; *Case II*: Annual maxima wet bulb temperature coincide/precedes by peak rain events. While *Case I* considers when extremes occur simultaneously or successively (e.g., multivariate-case), *Case II* deals with extremes combined with background conditions, which does not necessarily extreme by itself, amplifying

the overall impact (*e.g.*, sequential-case). We consider up to a week’s time lag since both extremes may not occur on the same day, and the response of pluvial floods within a week of occurrence of heat stress could be the part of the same large-scale phenomenon (Berghuijs et al., 2019; Rowe & Villarini, 2013).

## 2 Data and Methods

### 2.1 Data Collection

We obtain station-based daily meteorological records from the IMD (India Meteorological Department; <https://dsp.imdpune.gov.in/>) archived at 03:00 (08:30 IST) and 12:00 (17:30 IST) hour UTC from 1970-2017. Following the literature (Raymond et al., 2018; Zhang & Villarini, 2020), we sampled HHS from (See section 2.2) daily wet-bulb temperatures (WBT) sampled at 17:30 local time. We consider nine urbanized locations, representing seven homogeneous climatic zones (based on rainfall; Priyadarshi et al., 2020) of India (Figure 1b) with populations varying from 0.09 - 22.04 million.

### 2.2 Sampling of Compound Events

The high-pressure system, high humidity, and long-lasting atmospheric blocking are drivers of the emergence of HHS (Dubey et al., 2021; Saeed et al., 2021; Figure 1c). We define “multivariate compound” events as *Case I* when extreme WBT coincide or preceded by heavy precipitation events. Here multiple co-occurring hazards causing extreme impact (Zscheischler et al., 2020) are delineated using the POT approach. We initially compute several thresholds ranging from 95<sup>th</sup> to 99<sup>th</sup> percentiles at an increment of 0.5 from available meteorological records and later consider 96.5<sup>th</sup> percentile threshold, ensuring sufficient length of concurrent pairs across all sites (Figure S1 a-b). To ensure the independence of the selected extremes, we consider three days de-clustering periods (Barton et al., 2016). Next, as *Case II*, we sample “preconditioned compound” extreme when annual maxima (AMX) WBT precedes peak precipitation events within a *d-day* occurrence of the latter event. Here, AMX-WBT acts as a causal or triggering mechanism, whereas the peak precipitation, does not necessarily an extreme in a statistical sense, amplifies the overall impact (Zscheischler et al., 2020). Following the literature (Berghuijs et al., 2019; W. Zhang & Villarini, 2020), for both definitions (multivariate and preconditioned), we detect compound events when extreme *HHS* occurs within a *d-day* ( $d = 3, 5, \text{ and } 7$  days) before the extreme precipitation event.

### 2.3 Probabilistic Modelling

We used a series of probability distribution functions, such as Generalized Pareto (GP), Log-normal, Gamma, Generalized Extreme Value (GEV), Log-logistic distributions, and Kernel density functions for marginal distribution modelling of compound events (Tables S2 - S5). Due to its nonparametric nature, overall, the Kernel density function can represent extreme events reasonably well (Figures S2 – S5). To select the best distribution and to choose most parsimonious model, we evaluate the minimum AIC (Akaike Information Criteria) with cor-

rection for the small samples (Burnham & Anderson, 2003). Then performed the goodness-of-fit test using the Anderson Darling test (AD), which emphasizes discrepancies at the upper tail of a distribution.

We use parametric families of copulas to assess compound hazards associated with heat stress-pluvial floods. We estimate copula parameters using the maximum pseudo-likelihood approach (Genest et al., 1995). We determine the goodness-of-fit of copulas using the parametric bootstrap-based method employing Cramer-von Mises distance statistics, a measure of deviation between two continuous distribution functions (Rémillard, 2017; Supplementary Information SI.1). A large  $p$ -value indicates (Tables S6-S7) the best (offering the largest  $p$ -value) versus the next-best fit copulas have modelled the compound events well. Further, to check the credibility in modeling the upper tail of the compound heat stress-peak precipitation event, we evaluated an additional metric, *i.e.*, Upper Tail Ratio (UTR; Wietzke et al., 2020), to identify how well the selected copulas simulate the upper tail behavior of the joint distribution model. For this, first, we compute the observed UTR, which is defined as the ratio of the maximum compounding precipitation magnitude to the at site 10-year return level considering monsoon maxima precipitation (Section S1.2). Next, we calculate simulated UTR from copula-based simulated samples, in which we obtain the maximum precipitation quantiles using inverse CDF (distribution) transformation of the marginal distributions (Section S1.2; Tables S2 and S5). Finally, to investigate the feasibility of the selected copula family, we compare the observed versus simulated UTR of the best versus the next best copulas (Tables S8-S9). We select the copula family with the lowest relative bias and the uncertainty estimates evaluated through the interquartile range (Section S1.2; Figure S6).

## 2.4 Amplification Ratio

We propose a simple dimensionless index, Amplification Ratio (AR), to identify the hot spots experiencing heavy to very heavy precipitation preceded by heat stress. The index is motivated by the Compound hazard ratio (Ganguli & Merz, 2019) and represents a functional relationship linking at-site precipitation magnitude versus the *HHS*-driven compound precipitation. Mathematically,  $AR$  is the ratio between univariate return periods of peak rain events not preceded by *HHS*, and the conditional return periods of extreme precipitation compounded by the *HHS* events.

, where  $AR \in [0, \infty)$  (1)

An  $AR$  value larger (smaller) than 1 indicates amplifications (depreciation) in compound precipitation frequency relative to solely considering peak rain event. Here represents at-site return period for rainfall only events not preceded by *HSS* and defined as (Kim et al., 2003) , where is mean inter-arrival time between two consecutive rain only events; for *Case I*, , and for *Case II*,  $= 1$ , considering monsoon maxima precipitation events accounts for one event per year. represents total number of peak rain only events considering 96.5<sup>th</sup> percentile threshold,  $N$

denotes length of records (in years) and indicates the marginal distribution of rain only events. Tables S10-S11 and Figures S7-S8 suggest satisfactory fit of rainfall only events.

Likewise, the denominator, represents return period in a *CCP* framework assuming the condition when peak rain event exceeds the threshold given extreme WBT also exceeds a threshold (Brunner et al., 2016)

(2)

denotes mean inter-arrival time between consecutive compound events, ; indicates number of peak rain events preceded by the *HHS*. denotes CDF of peak precipitation events computed at 99<sup>th</sup> percentile (quantiles exceeding 1% of the time) of the sampled compound event pair, whereas denotes CDF of extreme WBT, which acts as a causal (conditional) driver for peak precipitation. is computed considering (i) the *likely* (i.e., 50<sup>th</sup> percentile *HHS* values) value from the sampled compound WBT events and (ii) considering  $T_W = 32^\circ\text{C}$ . indicates copula-based joint CDF.

## 2.5 Moisture Convergences during HHS-Peak Precipitation

To attribute physically, we compare the daily-averaged moisture transport on precipitation days preceded by HHS versus precipitation days not preceded by HHS for the years 1979-2018. The vertically integrated moisture transport (IVT) supplies a significant amount of moisture for the summer monsoon rainfall (Fasullo & Webster, 2003). We calculated the IVT as a composite of the vertical integral of eastward and northward water vapour flux provided by the ERA-Interim re-analysis products with a spatial resolution of  $0.75^\circ$  (Brands et al., 2017), whereas the mean IVT direction is evaluated using directional statistics (Mardia, 1975).

## 3 Results and Discussion

### 3.1 Pronounced Variability in Wet-bulb Temperature Trends

Our preliminary analysis over the selected urban areas (Figure 1a-b) shows that changes in median and extreme trends (annual maxima and the local 95<sup>th</sup> percentile time series over the 1970-2017 baseline) in WBT are more pronounced than DBT (Figure S9). The rate of change in DBT is less for most sites except Ahmedabad, where we observe a significant increasing trend in mean DBT. In contrast, Dehradun shows a significant declining trend in DBT with no significant increasing/decreasing trend for the WBT. Therefore, DBT alone is insufficient to capture the extreme *HHS* and may underestimate the associated risk. Our finding corroborates with Rogers et al. (2021) that suggests an amplification of *HHS* trend globally over densely urbanized locations leading to larger fraction of population exposure to humid heat as compared to *dry-heat*. Consequently, following earlier studies (Raymond et al., 2020; Zhang & Villarini, 2020), we have considered WBT an indicator of heat stress compounded by humidity.

### 3.2. Variability in Dependence Strength and Timing of Concurrent Occurrence

Next, to explore spatial heterogeneity in compound heat stress-pluvial flood hazards, we explore spatial dependence between drivers. The heat maps of dependence pattern (Figure S1a) for extreme at different levels versus time lags suggest the city located at a higher elevation and in temperate climate zone (*i.e.*, Dehradun; Figure 1a) show a dominant positive dependence between drivers. This could be because many mountainous and high-latitude regions of the northern hemisphere have reported warming-induced seasonal shifts in precipitation (Tamang et al., 2020). Further, the low-latitude coastal city, Panaji, located at a close proximity (7.5 km) to the Arabian Sea, shows concomitant increase in precipitation intensity with increase in *HHS*. The positive correlation at coastal cities is often linked to increased convection and local precipitation due to the combination of warm El Niño and Indian Ocean Dipole (IOD)-induced large-scale teleconnections (Ashok et al., 2004; Trenberth & Shea, 2005). We observe a mix of positive and negative correlations for remaining cities, with large proportions of negative correlations for Hyderabad and Bhubaneswar at different threshold levels. While in tropical urban areas, intense precipitation is reported with warming, the apparent negative correlation is explained by the humidity limitations at higher temperatures (Fowler et al., 2021). The lag period of 7 days and a threshold of 96.5<sup>th</sup> percentile capture the dependency pattern while ensuring sufficient sample lengths for multivariate hazard assessment (Figure S1b). Therefore, we have considered the threshold as 96.5<sup>th</sup> percentile and up to a week of time-lag for analyzing compound heat-pluvials in subsequent analyses.

To further investigate the seasonal variability of compound events, we compare the correlation values and their time of emergence across different seasons (Figure 2). While we note concurrence of *HHS*-precipitation is mainly limited to Southwest monsoon season (June – September), as confirmed by over 40% of samples in both cases. The spatial trend shows a distinct pattern for the western and eastern halves of the country. The positive dependence in western half indicates evidence of intense precipitation preceded by *HHS* (Kumar et al., 2010). The significant positive correlation (at 10% significance level) at Dehradun (Figure 2a) suggests possibility of robust amplification in peak discharge. In contrast, negative correlations over the eastern and the interior corridor of the sub-continent (*e.g.*, Hyderabad and Guwahati) are apparent. A likely explanation is extreme *HHS* occurrence during the break or weak spells of monsoon, leading to limited moisture availability in these areas (Ivanovich et al., 2021; Krishnan et al., 2009). Typically, during the southwest monsoon, higher values of WBTs are observed over north India compared to the southern peninsula, with larger diurnal variability at the east coast in contrast to smaller variations at the west coast (Reddy, 1976). The scatter plot of peak precipitation versus the *HHS* (Figure S10) further confirms notable heat stress over north India (Delhi) and eastern coast (Kolkata), where the WBT tend to attain or even exceed the WBT threshold of 30°C, triggering thermal discomfort and

slowdown in labour productivity (Dasgupta et al., 2021).

The UTR distribution of Case I shows 7 out of 9 cities tends to be more intense ( $>1 - 1.3$ ), indicating major flooding (Figure S11). For Case II, one city shows bankfull conditions with UTR value of 0.56, followed by five cities show minor to moderate flooding with UTR ranges from 0.6 – 1 (Villarini et al., 2014). For Dehradun, the UTR value is more than one in both cases, indicating susceptibility to major flooding. The larger value of UTR for Case I compared to Case II could be because in former, both drivers are extremes by themselves, whereas for the latter extreme WBT, acts as a triggering mechanism for peak precipitation, where the rain event does not necessarily be an extreme.

### 3.2 Trends in Pluvial Frequency and its Amplification

We identify “hotspot” cities with larger amplifications in peak precipitation in a *CCP* framework, assuming the occurrence of peak precipitation preceded by the extreme WBT. Extreme precipitations are identified from the 99<sup>th</sup> percentile of the flood peak distribution from compound event pairs, considering two scenarios of *HHS* as physical covariates: the *likely* scenario represented by the  $T_W > 50^{\text{th}}$  percentile of sampled *HHS*, and the extreme  $T_W$  scenario considering  $T_W > 32^{\circ}\text{C}$ , the upper limit of labour productivity. To provide a regional view, we coined a normalized metric, *AR* statistics that provide an information of how much larger (or smaller) are the compound flood peak distribution than the at site peak precipitation frequency without considering *HHS*. Although considering the *likely* scenario (Figure 3a), only a few locations (one site in Case I and four sites in Case II) show perceptible changes with  $AR > 1$ , considering extreme  $T_W$  scenario, the majority of sites report considerable shortening of the return period. The largest amplifications are observed for Mumbai and Panaji, followed by Ahmedabad – all three cities are close to the ocean, which indicates the coastal cities are at greater risk of heat stress-driven pluvial flood risk.

We further compare the return period corresponding to peak rainfall *not* preceded by *HHS* versus the return period corresponding to heat-stress-driven rain events for the extreme  $T_W$  scenario (Figure. 3b). The scatter plot is divided into four quadrants, considering a threshold return period of 25-year, which is adequate to flood small to medium-sized catchments (CWC, 2012). The cities lie in quadrants II and IV are exposed to larger risk, manifested by considerable shortening of *HHS*-driven rain events, even down to 2-year (*e.g.*, Ahmedabad and Panaji in Fig. 3b) compared to at-site extreme precipitation frequency, which are *not* preceded by *HHS*. This demonstrates peak rainfall episodes compounded by *HSS* tend to become intense and frequent, which may be underestimated by solely considering extreme precipitation. Interestingly, compared to Case II, the frequency amplification trends in Case I are modest, with the maximum value close to 3, and often characterized by depreciation ( $AR < 1$ ). This could be because in Case I, each variables in the *AR* metric, including its drivers in the denominator, are extreme by itself. In contrast, in Case II, the *AR* metric is determined by the ratio of design rain events of seasonal (June-September) maxima precipitation to the *HSS*-driven peak precipitation, where

the latter variable may not be necessarily extreme. However, a combination of (several) modest values augmented by background conditions may result in an extreme impact (Pescaroli & Alexander, 2018).

### 3.3 Precipitation Frequency and Moisture Flux during Concurrent Event

To identify underlying causes of precipitation amplification, we compare the mean moisture transport of precipitation days compounded by HHS events versus moisture transport of precipitation days *not* preceded by HHS events (Figure 4a-b). The mean moisture convergence shows an anomalous anticyclonic pattern in the Northern part of India (Figure 4), a signature of atmospheric blocking during hot days (Dubey et al., 2021). During wet spells, the anomalous wind patterns caused by shorter blocking events pushed monsoon rains north and west, resulting in heavy rains in these areas. Below 17° N at Southern India, moisture movement arises from the Arabian ocean towards the Bay of Bengal on the day of HHS. The composites show accumulating moisture flux, which tends to be more pronounced ( $\sim 550 \text{ kgm}^{-1}\text{s}^{-1}$  of IVT) over the region during precipitation days preceded by HHS. In contrast, the moisture flux, during precipitation days *not* preceded HHS, is relatively lower than the former two cases. A substantial moisture convergence is apparent in Case I than Case II on precipitation days preceded by *HHS*. Mechanistically, it appears that extreme WBT in the tropics augments convective instability, which potentially enhances atmospheric convection and precipitation (Zhang et al., 2021). To explain further, we compare histograms of the rainfall frequency versus the magnitude for both cases. For Case I, a long tail on a higher magnitude of rainfall together with a notable shift in the mean rainfall suggest a “changed symmetry” associated with rain events preceded by HHS (Figure 4a, extreme right), which indicates an intensification of compound rain events. For Case II, no such evidence of shifted mean (towards higher rainfall) is apparent for compound rain events (Figure 4b, extreme right).

## 4 Conclusions

We demonstrate the heat stress-pluvial compound flood potentials of urban agglomerates of India via two cases: in *Case I*, both drivers were considered as extreme (POT WBT and POT precipitation) where severe heat stress is either coincided or preceded by the extreme rain events, whereas in *Case II*, annual maxima WBT was considered as a preconditioned driver triggering peak rain event within a limited time window. Recently, a few studies have detected the cascading impact of *HHS* (i.e., preconditioned driver) on extreme precipitation occurrence (i.e., responder); however, such efforts are mostly confined to mid-to-high latitudes (Fowler et al., 2021; Zhang & Villarini, 2020) and sub-tropical continents (Bui et al., 2019; Ning et al., 2022; You & Wang, 2021). While using re-analysis products, Zhang & Boos (2021) showed susceptibility of heavy to very heavy precipitation about half of the Global land areas between 50°N and 50°S coincided or immediately following extreme WBT, very few studies have explored compound flood potentials and associated hazards of *HSS*-coupled-

rainfall extremes, especially over tropics, one of the vulnerable regions in Earth’s climate system (Lenton et al., 2008).

Our analyses reveal a spatially coherent dependence structure for the cities located across western versus eastern corridors of the country - a statistically significant decreasing dependence strength is apparent for cities located across the east, whereas the urban areas located across the west show (insignificant) positive dependence. While a positive dependence suggests a more frequent and extreme rainfall compounded by *HHS*, the negative dependence between drivers indicates the possibility of reduced peak magnitude of pluvials. Barring the strength of dependence between drivers, the spatial distribution of UTR suggests moderate to severe flooding due to preceding *HHS* events. In particular, coastal cities are more exposed to heat stress; which is alarming since in warming climate with the advent of local sea-level rise, especially in tropics (Hooijer & Vernimmen, 2021), more precipitation may increase the vulnerability of low-lying coasts owing to coastal compound flooding (Dhiman et al., 2018; Fang et al., 2021).

Due to a limited number of station-based observations, while spatiotemporal coverage of records remains constrained for this study, our proof-of-principal framework could extend to any geographical region to identify hotspots of humid heat stress-pluvial flooding using observations and climate model output. Further, considering different sources of uncertainty in bivariate framework, we assume the effect of changes in the time series are not large. Although our initial case study is confined to selected urban locations of India, the obtained insights provide a new perspective for understanding the response of compound *HHS*-pluvial extremes, which will be helpful for risk management, flash flood forecast, and insurances. We may expect enhanced *HHS*-precipitation coupling with significant social and economic repercussions as climate shocks increase (IPCC - SPM, 2022). Future assessments are needed to understand the consequences of anthropogenic forcing on compound *HHS*-pluvial extremes unveiling the intricate feedback processes of the climate system and preparing resilience to extreme events.

## 5 Data availability

Station-based meteorological records are procured from the IMD (India Meteorological Department; <https://dsp.imdpune.gov.in/>). The population data is obtained from the Census India website, available freely at (<https://censusindia.gov.in/>). The digital elevation models (DEM) of India are obtained from Global 30 Arc-Second Elevation (GTOPO30) available at: <https://www.usgs.gov/centers/eros/science/usgs-eros-archive-digital-elevation-global-30-arc-second-elevation-gtopo30>. The IVT records are obtained from the European Centre for Medium-Range Weather Forecasts (ECMWF)’s ERA-Interim product available at a daily resolution via the web-link: <https://apps.ecmwf.int/datasets/data/interim-full-daily/levtype=sfc/>

## Acknowledgments

The work did not receive any significant funding. However, we sincerely acknowledge the computing facility provided by the Indian Institute of Technology Kharagpur. Sucheta Pradhan is supported through MHRD scholarship from the government of India to carry out the Master's thesis at IIT Kharagpur.

**Open Research** The urban population data could be retrieved from the Census of India website, available at <https://censusindia.gov.in/>. The digital elevation models (DEM) of India are obtained from Global 30 Arc-Second Elevation (GTOPO30) archive available at: <https://www.usgs.gov/centers/eros/science/usgs-eros-archive-digital-elevation-global-30-arc-second-elevation-gtopo30>. The IVT records are obtained from the European Centre for Medium-Range Weather Forecasts (ECMWF)'s ERA-Interim product available at a daily resolution through the web archive: <https://apps.ecmwf.int/datasets/data/interim-full-daily/levtype=sfc/>

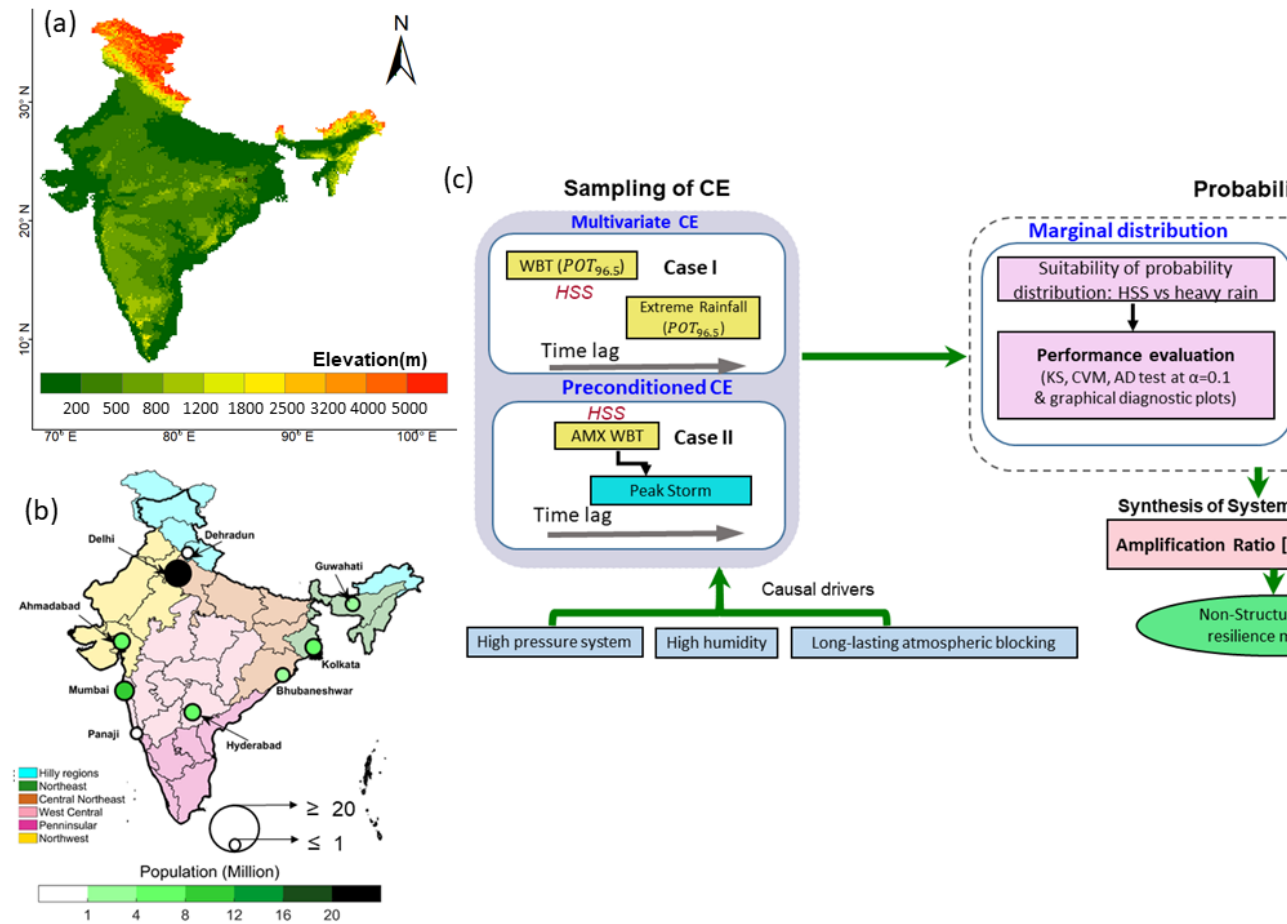


**Figure 1:** (a) Elevation profile of India. The digital elevation models (DEM) of India are obtained from Global 30 Arc-Second Elevation (GTOPO30) database available at approximately 1 km resolution. The elevation map of India is projected using spatial analysis software Arc GIS Desktop version 10.8.1. (b) Map of India showing 9 cities with their population and seven homogeneous climatic zones (rainfall). Size and shade of the circles is proportional to population density, the lighter (dark) shade and smaller (larger) circles represent smaller (higher) population density. The projected population for 2020 was calculated using previous census record. (c) Flowchart summarizing the workflow, where CE = compound event, WBT = wet-bulb temperature,  $POT_{96.5}$  = peak over threshold level (96.5), AMX = Annual Maxima, KS = Kolmogorov-Smirnov, CVM=Cramer-von Mises, AD = Anderson Darling,  $\alpha$  = level of significance,  $T_{Q|WBT}$  = Conditional return period corresponds to heat-stress induced peak rain event,  $T_Q$  = Return period corresponds to peak rain event NOT preceded by heat stress.

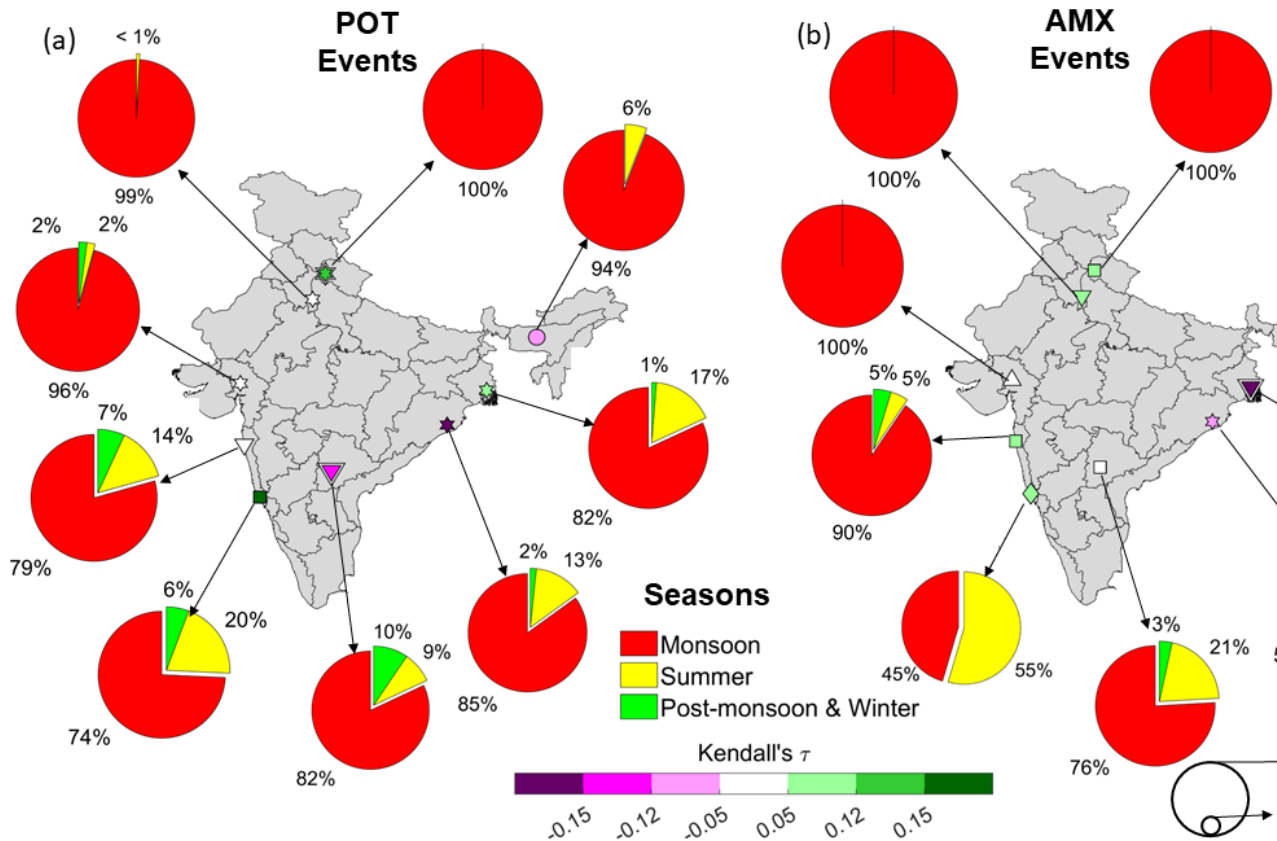


**Figure 2:** Spatial distribution of strength of dependence between drivers with their selected copula family for Case I (POT) and Case II (AMX). Pie Charts show the time (season) of concurrence of the compound extreme. The shape of marker denotes selected copula types – markers with double boundary indicate statistically significant dependence at 10% level.

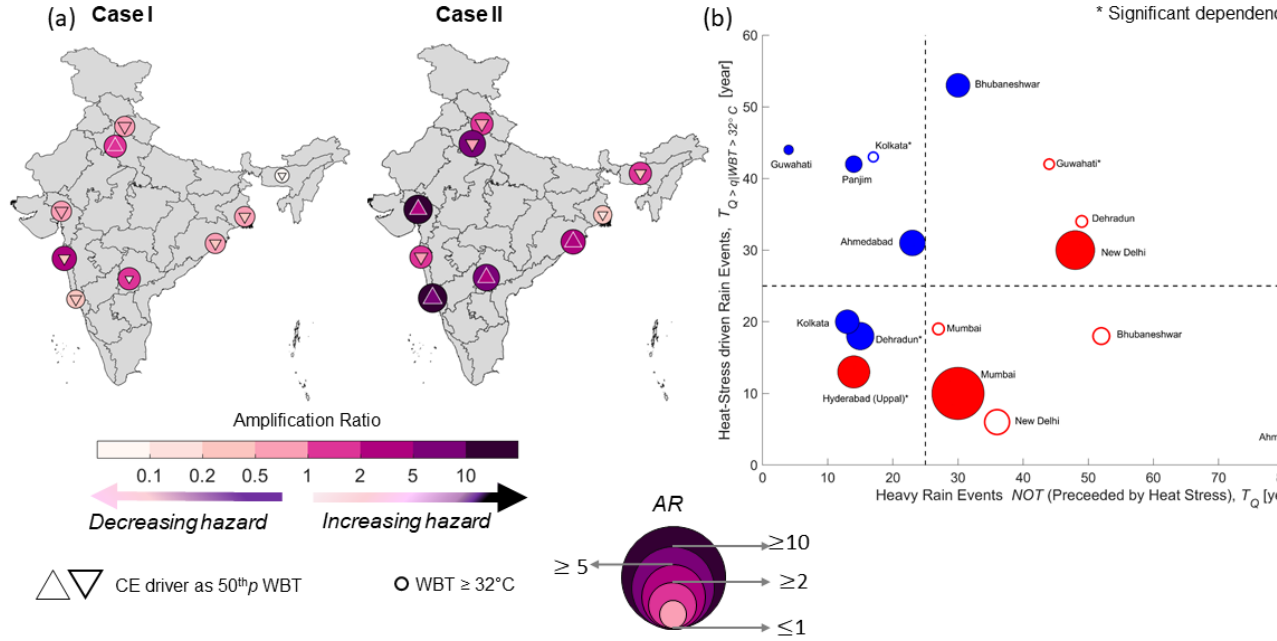


**Figure 3:** (a) Spatial distributions of Amplification Ratio,  $AR$ . The up (down) triangles represents *likely* scenario, i.e.,  $T_w > 50^{\text{th}}$  percentile of sampled HHS, whereas circles indicates extreme  $T_w$  scenario, considering  $T_w > 32^\circ\text{C}$ . Further, up triangle indicates an amplification, whereas down triangle denotes depreciation. (b) Scatter plot shows the relationship between univariate return period for peak rainfall event *not* preceded by HHS and the calculated return period in a *CCP* framework indicating heat-stress-driven peak rain events for the extreme scenario. The filled circles indicate Case I and the empty circles represents Case II. Red and blue colour circles represent amplification and depreciation, respectively. The locations with significant dependence are marked with asterisk (\*).

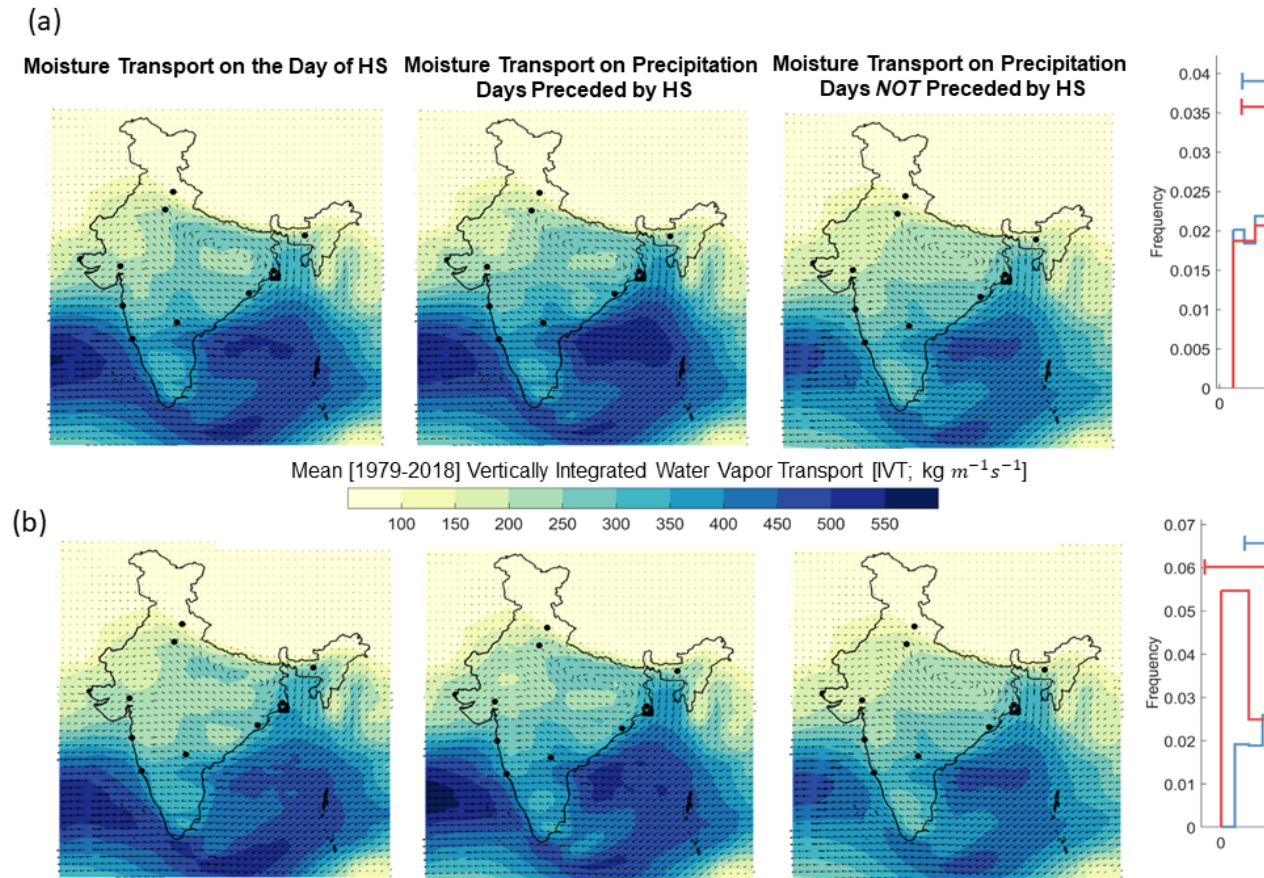


**Figure 4:** Daily-averaged moisture transport on the day of HHS, on the precipitation days preceded by and not preceded by HHS for (a) Case I and (b) Case II. Histograms of the rainfall frequency versus the rainfall magnitude for (a; *extreme right*) Case I and (b; *extreme right*) Case II.

#### References

Agilan, V., & Umamahesh, N. V. (2017). What are the best covariates for developing non-stationary rainfall Intensity-Duration-Frequency relationship? *Advances in Water Resources*, 101, 11–22.

Ashok, K., Guan, Z., Saji, N. H., & Yamagata, T. (2004). Individual and Combined Influences of ENSO and the Indian Ocean Dipole on the Indian Summer Monsoon. *Journal of Climate*, 17(16), 3141–3155.

Berghuijs, W. R., Allen, S. T., Harrigan, S., & Kirchner, J. W. (2019). Growing Spatial Scales of Synchronous River Flooding in Europe. *Geophysical Research Letters*, 46(3), 1423–1428.

Brands, S., Gutiérrez, J. M., & San-Martín, D. (2017). Twentieth-century atmospheric river activity along

the west coasts of Europe and North America: algorithm formulation, reanalysis uncertainty and links to atmospheric circulation patterns. *Climate Dynamics*, 48(9–10), 2771–2795.

Bui, A., Johnson, F., & Wasko, C. (2019). The relationship of atmospheric air temperature and dew point temperature to extreme rainfall. *Environmental Research Letters*, 14(7), 074025.

Burnham, K. P., & Anderson, D. R. (2003). *Model selection and multimodel inference: a practical information-theoretic approach*. Springer.

CREC (Centre for Research on the Epidemiology of Disasters). (2018). *Review of Disaster Events* (pp. 1–6). Belgium: Université catholique de Louvain. Retrieved from <https://www.cred.be/CWC> (Central Water Commission, 2012). *Handbook for flood protection, anti-erosion and river training works*. Flood management organization, New Delhi.

Dasgupta, S., Maanen, N. van, Gosling, S. N., Piontek, F., Otto, C., & Schleussner, C.-F. (2021). Effects of climate change on combined labour productivity and supply: an empirical, multi-model study. *The Lancet Planetary Health*, 5(7), e455–e465.

Davis, R. E., McGregor, G. R., & Enfield, K. B. (2016). Humidity: A review and primer on atmospheric moisture and human health. *Environmental Research*, 144, 106–116.

Dhiman, R., VishnuRadhan, R., Eldho, T. I., & Inamdar, A. (2018). Flood risk and adaptation in Indian coastal cities: recent scenarios. *Applied Water Science*, 9(1), 5.

Dubey, A. K., Kumar, P., Saharwardi, M. S., & Javed, A. (2021). Understanding the hot season dynamics and variability across India. *Weather and Climate Extremes*, 32, 100317.

Fang, J., Wahl, T., Fang, J., Sun, X., Kong, F., & Liu, M. (2021). Compound flood potential from storm surge and heavy precipitation in coastal China: dependence, drivers, and impacts. *Hydrology and Earth System Sciences*, 25(8), 4403–4416.

Fasullo, J., & Webster, P. J. (2003). A hydrological definition of Indian monsoon onset and withdrawal. *Journal of Climate*, 16(19), 3200–3211.

Fechter-Leggett, E. D., Vaidyanathan, A., & Choudhary, E. (2016). Heat Stress Illness Emergency Department Visits in National Environmental Public Health Tracking States, 2005–2010. *Journal of Community Health*, 41(1), 57–69.

Fischer, E. M., & Knutti, R. (2015). Anthropogenic contribution to global occurrence of heavy-precipitation and high-temperature extremes. *Nature Climate Change*, 5(6), 560–564.

Fowler, H. J., Lenderink, G., Prein, A. F., Westra, S., Allan, R. P., Ban, N., et al. (2021). Anthropogenic intensification of short-duration rainfall extremes. *Nature Reviews Earth & Environment*, 2(2), 107–122.

Ganguli, P., & Merz, B. (2019). Extreme Coastal Water Levels Exacerbate Fluvial Flood Hazards in Northwestern Europe. *Scientific Reports*, 9(1), 13165.

Hooijer, A., & Vernimmen, R. (2021). Global LiDAR land elevation data reveal greatest sea-level rise vulnerability in the tropics. *Nature Communications*, 12(1), 3592.

Im, E.-S., Pal, J. S., & Eltahir, E. A. (2017). Deadly heat waves projected in the densely populated agricultural regions of South Asia. *Science Advances*, 3(8), e1603322.

Ivanovich, C., Horton, R. M., & Sobel, A. H. (2021). Extreme Humid Heat during South Asian Summer Monsoon Breaks. In *AGU Fall Meeting 2021*. AGU.

Kim, T.-W., Valdés, J. B., & Yoo, C. (2003). Nonparametric Approach for Estimating Return Periods of Droughts in Arid Regions. *Journal of Hydrologic Engineering*, 8(5), 237–246.

Krishnamurthy, C. K. B., Lall, U., & Kwon, H.-H. (2009). Changing Frequency and Intensity of Rainfall Ex-

tremes over India from 1951 to 2003. *Journal of Climate*, 22(18), 4737–4746.

Krishnan, R., Kumar, V., Sugi, M., & Yoshimura, J. (2009). Internal feedbacks from monsoon–midlatitude interactions during droughts in the Indian summer monsoon. *Journal of the Atmospheric Sciences*, 66(3), 553–578.

Kumar, V., Jain, S. K., & Singh, Y. (2010). Analysis of long-term rainfall trends in India. *Hydrological Sciences Journal*, 55(4), 484–496.

Lenton, T. M., Held, H., Kriegler, E., Hall, J. W., Lucht, W., Rahmstorf, S., & Schellnhuber, H. J. (2008). Tipping elements in the Earth’s climate system. *Proceedings of the National Academy of Sciences*, 105(6), 1786–1793.

Mardia, K. V. (1975). Statistics of directional data. *Journal of the Royal Statistical Society: Series B (Methodological)*, 37(3), 349–371.

Masson-Delmotte, V., Zhai, P., Pirani, A., Connors, S. L., Péan, C., Berger, S., et al. (Eds.). (2021). *Climate Change 2021: The Physical Science Basis. Contribution of Working Group I to the Sixth Assessment Report of the Intergovernmental Panel on Climate Change*. Cambridge University Press.

Nelsen, R. B. (2013). *An introduction to copulas* (Vol. 139). Springer.

Ning, G., Luo, M., Zhang, W., Liu, Z., Wang, S., & Gao, T. (2022). Rising risks of compound extreme heat-precipitation events in China. *International Journal of Climatology*, Doi: 10.1002/joc.7561.

Pescaroli, G., & Alexander, D. (2018). Understanding compound, interconnected, interacting, and cascading risks: a holistic framework. *Risk Analysis*, 38(11), 2245–2257.

Priyadarshi, N., Bandyopadhyay, S., Chowdary, V. M., Chandrasekar, K., Chockalingam, J., Raj, U., & Jha, C. S. (2020). Segmentation-based approach for trend analysis and structural breaks in rainfall time series (1851–2006) over India. *Hydrological Sciences Journal*, 65(9), 1583–1595.

Raymond, C., Matthews, T., & Horton, R. M. (2020). The emergence of heat and humidity too severe for human tolerance. *Science Advances*, 6(19), eaaw1838.

Reddy, S. J. (1976). Wet bulb temperature distribution over India. *Mausam*, 27(2), 167–172.

Risser, M. D., & Wehner, M. F. (2017). Attributable Human-Induced Changes in the Likelihood and Magnitude of the Observed Extreme Precipitation during Hurricane Harvey. *Geophysical Research Letters*, 44(24), 12,457–12,464.

Rogers, C. D., Ting, M., Li, C., Kornhuber, K., Coffel, E. D., Horton, R. M., et al. (2021). Recent Increases in Exposure to Extreme Humid-Heat Events Disproportionately Affect Populated Regions. *Geophysical Research Letters*, 48(19), e2021GL094183.

Rohini, P., Rajeevan, M., & Srivastava, A. K. (2016). On the Variability and Increasing Trends of Heat Waves over India. *Scientific Reports*, 6(1), 26153.

Rosenzweig, B. R., McPhillips, L., Chang, H., Cheng, C., Welty, C., Matsler, M., et al. (2018). Pluvial flood risk and opportunities for resilience. *Wiley Interdisciplinary Reviews: Water*, 5(6), e1302.

Rowe, S. T., & Villarini, G. (2013). Flooding associated with predecessor rain events over the Midwest United States. *Environmental Research Letters*, 8(2), 024007.

Saeed, F., Schleussner, C.-F., & Ashfaq, M. (2021). Deadly Heat Stress to Become Commonplace Across South Asia Already at 1.5°C of Global Warming. *Geophysical Research Letters*, 48(7), e2020GL091191.

Sharma, S., & Mujumdar, P. (2017). Increasing frequency and spatial extent of concurrent meteorological droughts and heatwaves in India. *Scientific Reports*, 7(1), 15582.

Stone Jr, B., Mallen, E., Rajput, M., Gronlund, C. J., Broadbent, A. M., Krayenhoff, E. S., et

al. (2021). Compound Climate and Infrastructure Events: How Electrical Grid Failure Alters Heat Wave Risk. *Environmental Science & Technology*, 55(10), 6957–6964. Tamang, S. K., Ebtehaj, A. M., Prein, A. F., & Heymsfield, A. J. (2020). Linking global changes of snowfall and wet-bulb temperature. *Journal of Climate*, 33(1), 39–59. Trenberth, K. E., & Shea, D. J. (2005). Relationships between precipitation and surface temperature. *Geophysical Research Letters*, 32(14). Doi: 10.1029/2005GL022760. You, J., & Wang, S. (2021). Higher probability of occurrence of hotter and shorter heat waves followed by heavy rainfall. *Geophysical Research Letters*, 48(17), e2021GL094831. Villarini, G., Goska, R., Smith, J. A., & Vecchi, G. A. (2014). North Atlantic tropical cyclones and US flooding. *Bulletin of the American Meteorological Society*, 95(9), 1381–1388. Zhang, W., & Villarini, G. (2020). Deadly compound heat stress-flooding hazard across the central United States. *Geophysical Research Letters*, 47(15), e2020GL089185.

Zhang, Y., & Boos, W. R. (2021). Risk of intense precipitation accompanying extreme wet-bulb temperatures. In *AGU Fall Meeting 2021*. AGU.

Zhang, Y., Held, I., & Fueglistaler, S. (2021). Projections of tropical heat stress constrained by atmospheric dynamics. *Nature Geoscience*, 14(3), 133–137.

Zscheischler, J., Martius, O., Westra, S., Bevacqua, E., Raymond, C., Horton, R. M., et al. (2020). A typology of compound weather and climate events. *Nature Reviews Earth & Environment*, 1(7), 333–347.



*Geophysical Research Letters*

Supporting Information for

**Multivariate Approach Reveals a Higher Likelihood of Compound Heat Stress-Pluvial Floods in Urban India**

Poulomi Ganguli<sup>1</sup>, Sucheta Pradhan<sup>1</sup>

<sup>1</sup>Agricultural and Food Engineering Department, Indian Institute of Technology Kharagpur, India

**Contents of this file**

Text S1

Figures S1 to S11

Tables S1 to S11

## Text S1

### SI.1 Goodness-of-fit of Copulas using Parametric Bootstrap Method

We employ the parametric bootstrap-based goodness-of-fit test as suggested by Rémillard (2017) to select the best copula family. Parametric bootstrap procedure is described as below:

For large integer resamples  $N$  ( $N \gg n$ , where  $n$  is the sample length) generated from the copula families, we perform the following test statistics:

1. Compute  $C_n$  and estimate the copula parameter  $\phi$  with  $\phi_n = T_n(U_{1,n}, \dots, U_{n,n})$ , where  $T_n$  represents a deterministic function with expression  $T_n = \psi(P_n)$ ,  $U_{1,n}, \dots, U_{n,n}$  denote  $n$ -dimensional ( $n=2$ ) rank order transformed variables or the pseudo observations and  $P_n$  is the CDF of rank-ordered transformed variable vector given by,

$$P_n = \sqrt{n(C_n - C_{\phi_n})} \quad (S1)$$

Where  $C_n(U_{i,n})$  is the CDF of the empirical copula and  $C_{\phi_n}(U_{i,n})$  represent CDF estimated from the parametric copula family. For two dimensional case, the empirical copula,  $C_n(u_1, u_2)$  is estimated from the following expression

$$C_n(u_1, u_2) = \frac{1}{n} \sum_{i=1}^n \mathbf{1}\{\hat{U}_{i,1} \leq u_1, \hat{U}_{i,2} \leq u_2\} = \frac{1}{n} \sum_{i=1}^n \mathbf{1}\left\{\frac{R_{i,1}}{n+1} \leq u_1, \frac{R_{i,2}}{n+1} \leq u_2\right\} \quad (S2)$$

$$\mathbf{u} = \{u_1, u_2\} \in [0, 1]^2$$

Where  $R_{i,1}$  and  $R_{i,2}$  are the rank of the observation and

$$U_{i,1} = \frac{1}{n+1} \sum_{j=1}^n \mathbf{1}\{X_j \leq X_i\}, \quad U_{i,2} = \frac{1}{n+1} \sum_{j=1}^n \mathbf{1}\{X_j \leq X_i\} \quad \forall i = \{1, 2, \dots, n\}$$

2. Compute the value of empirical Crámer von Mises distance (CvMD) statistics  $S_{emp}$ , which is an integrated squared difference between CDF calculated from empirical copula and the parametric family of copula.

$$S_{emp} = \int_{[0,1]^d} P_n^2(u) dC_n(u) = \sum_{i=1}^n \{C_n(U_{i,n}) - C_{\phi_n}(U_{i,n})\}^2 \quad (S3)$$

3. For some large integer  $N$ , repeat the following steps for every  $k \in \{1, \dots, N\}$ :

- a. Generate a random sample  $Y_{i,n}^{(k)}, \dots, Y_{n,n}^{(k)}$  from distribution  $C_{\emptyset,n}$  and compute the pseudo-observations  $U_{i,n}^{(k)} = \mathbf{R}_{i,n}^{(k)} / (n + 1)$ , where  $R_{i,n}^{(k)}, \dots, R_{n,n}^{(k)}$  are the associated rank vectors of  $Y_{i,n}^{(k)}, \dots, Y_{n,n}^{(k)}$ .
- b. Estimate copula parameter  $\varphi$  with  $\varphi_n^{(k)} = T_n(U_{1,n}^{(k)}, \dots, U_{n,n}^{(k)})$ , where  $U_{1,n}^{(k)}, \dots, U_{n,n}^{(k)}$  are the simulated ranked data. Compute CDF from the simulated ranked sample,  $C_n^{(k)}(u)$

$$C_n^{(k)}(u) = \frac{1}{n} \sum_{i=1}^n \mathbf{1}(U_{i,n}^{(k)} \leq u), \quad u \in [0,1]^d \quad (\text{S4})$$

- c. Compute corresponding CvMD

$$S_{boot}^{(k)} = \sum_{i=1}^n \left\{ C_n^{(k)}(U_{i,n}^{(k)}) - C_{\varphi_n^{(k)}}(U_{i,n}^{(k)}) \right\}^2 \quad (\text{S5})$$

The critical value of test statistic at  $\alpha$  significance level based on  $S_n$  is given as  $S_{boot, [(1-\alpha)n]; n}^k$ , where  $\lfloor x \rfloor$  denotes the integer part of  $x$ . An approximate p-value for the test is then given by

$$\sum_{k=1}^N \mathbf{1} \frac{(S_{boot}^k > S_{emp})}{N}.$$

We compute the critical value of the test at 5% significance level. Based on the largest p-value obtained through  $N = 500$  bootstrap resamples, we have identified the best fit copula family. Other than the parametric bootstrap method, we employed the upper tail ratio to choose the suitable copula family (UTR; See section SI.2), which is the ratio between pluvial flood hazard component represented by heat- stress-driven compound precipitation and the at-site 10-year seasonal maxima precipitation. Next, we compare the observed UTR obtained from the historical precipitation series (See Eq. S6 in section SI.2) versus the simulated UTR (See Eq. S7 in section SI.2) obtained from the best and the next-best fit copula family. Finally, we select the suitable copula family that offers the lowest percentage bias (denoted with PBias) and the minimum uncertainty estimated through the interquartile range between the two copula families.

## SI.2 Selection of Copulas based on Goodness-of-fit test and Upper Tail Ratios

We compare the copula performance to fit the Upper Tail Ratio (UTR; Wietzke et al., 2020) of the extreme precipitation to ensure the heavy tail behavior is simulated adequately well by the selected copula. For this, we calculate the observed UTR and the simulated UTR using the following expression:

$$UTR_{observed} = \frac{\text{Maximum compounding precipitation depth within a week of occurrence of heat stress}}{\text{Atsite 10 year return level considering seasonal maxima precipitation}} \quad (S6)$$

$$UTR_{simulated} = \frac{\text{Mximum precipitation depth synthetically simulated by selected copula family in a n=500 bootsrap run}}{\text{Atsite 10 year return level considering seasonal maxima precipitation}} \quad (S7)$$

In Eqs. S6 and S7 we consider the seasonal maxima precipitation during June-September months at the denominator since the southwest summer monsoon season is the largest contributor of total annual rainfall in India (Soman & Kumar, 1990).

Further, following earlier studies (Rowe & Villarini, 2013; Villarini & Smith, 2010), we normalized Eqs. S6 and S7 using at-site 10-year pluvial flood return level. The 10-year flood is a commonly used threshold to distinguish properties of the upper tail of flood distributions (see, e.g., O'Connor & Costa, 2004; Villarini et al., 2011). We calculate the PBias of the best fit and the next best fitted copula families using Eqs. S6-S7. Finally, we select the copula based on the minimum PBias and the lower inter Quartile Range (IQR) (i.e., the difference between 25th and 75th quantile) values between the best fit and the second-best fit copula families.

$$PBias = \frac{UTR_{observed} - UTR_{simulated}}{UTR_{observed}} \quad (S8)$$

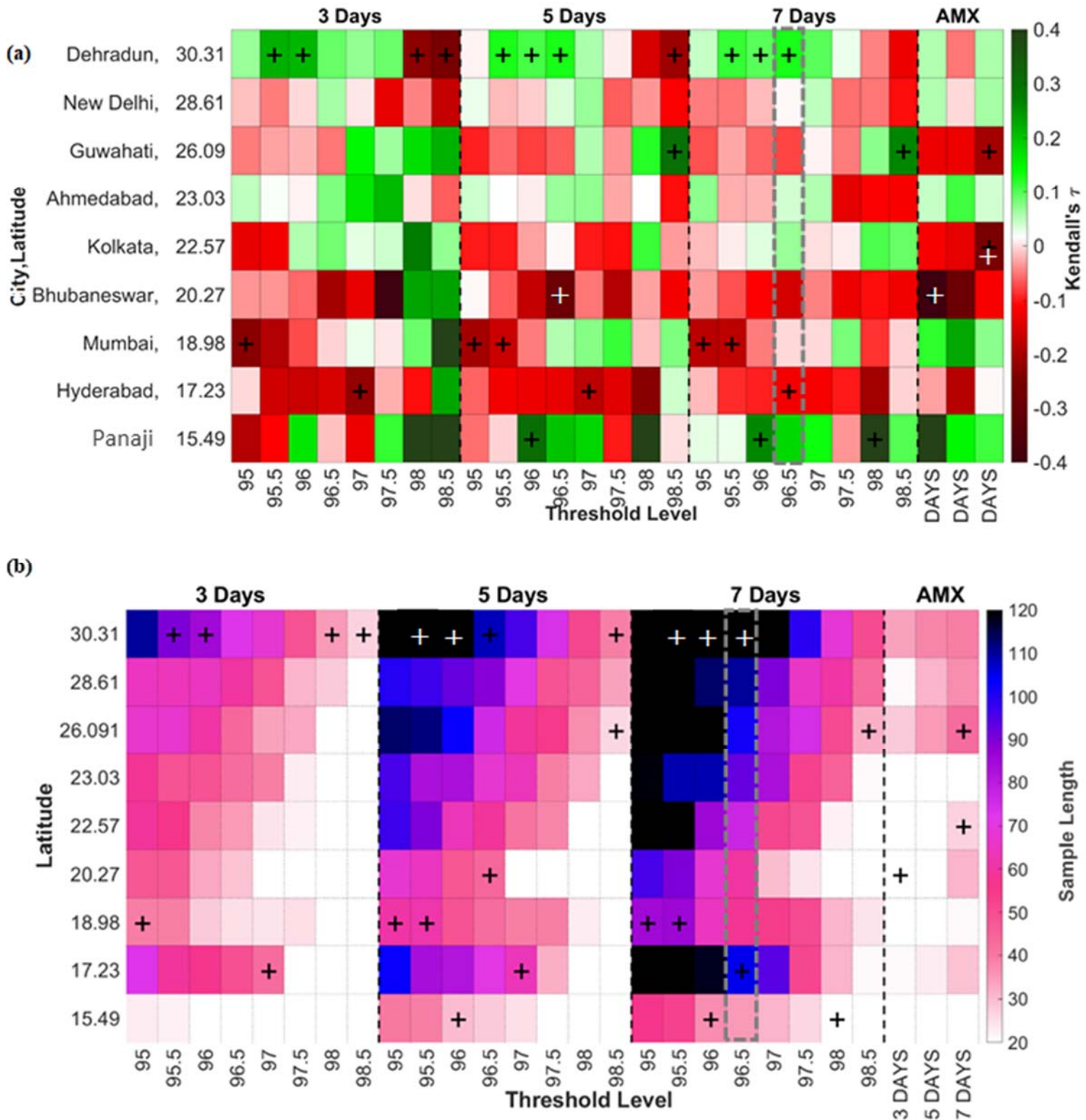


**Figure S1.** Variability of (a) dependence pattern and (b) sample length considering different extreme level and time lag. The selected time window and extreme level, i.e., 96.5<sup>th</sup> percentile and 7-day time lag, is marked with dotted rectangle in gray. The statistical significance of dependence strength is evaluated at 10% significance level i.e., p-value < 0.10 and marked with '+' symbol.

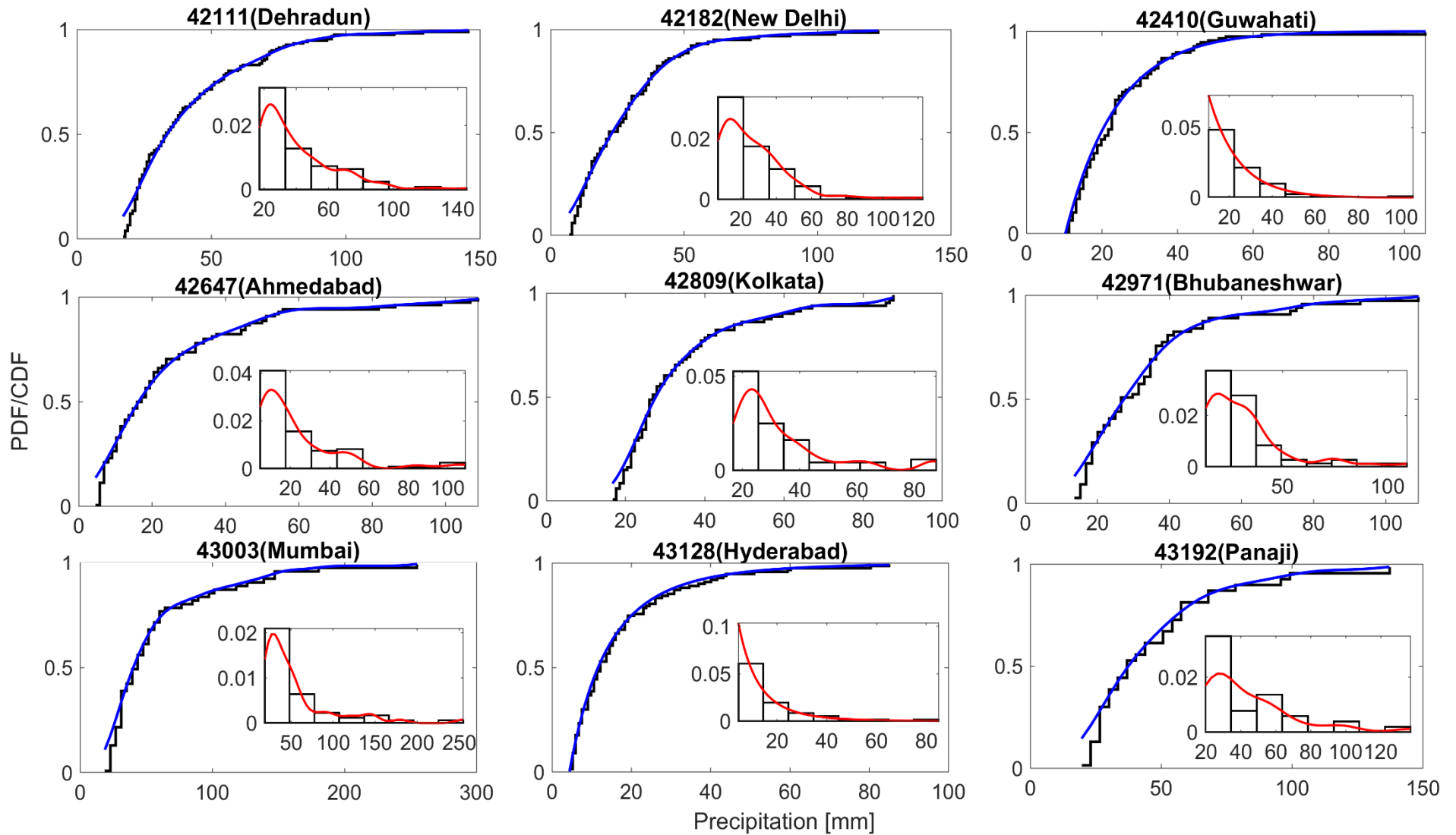


**Figure S2.** Distribution fits for Precipitation for Case I (POT). The empirical CDF is shown in solid thick black lines, whereas the fitted theoretical distribution is shown using blue lines. The inset shows the fit of probability density function.

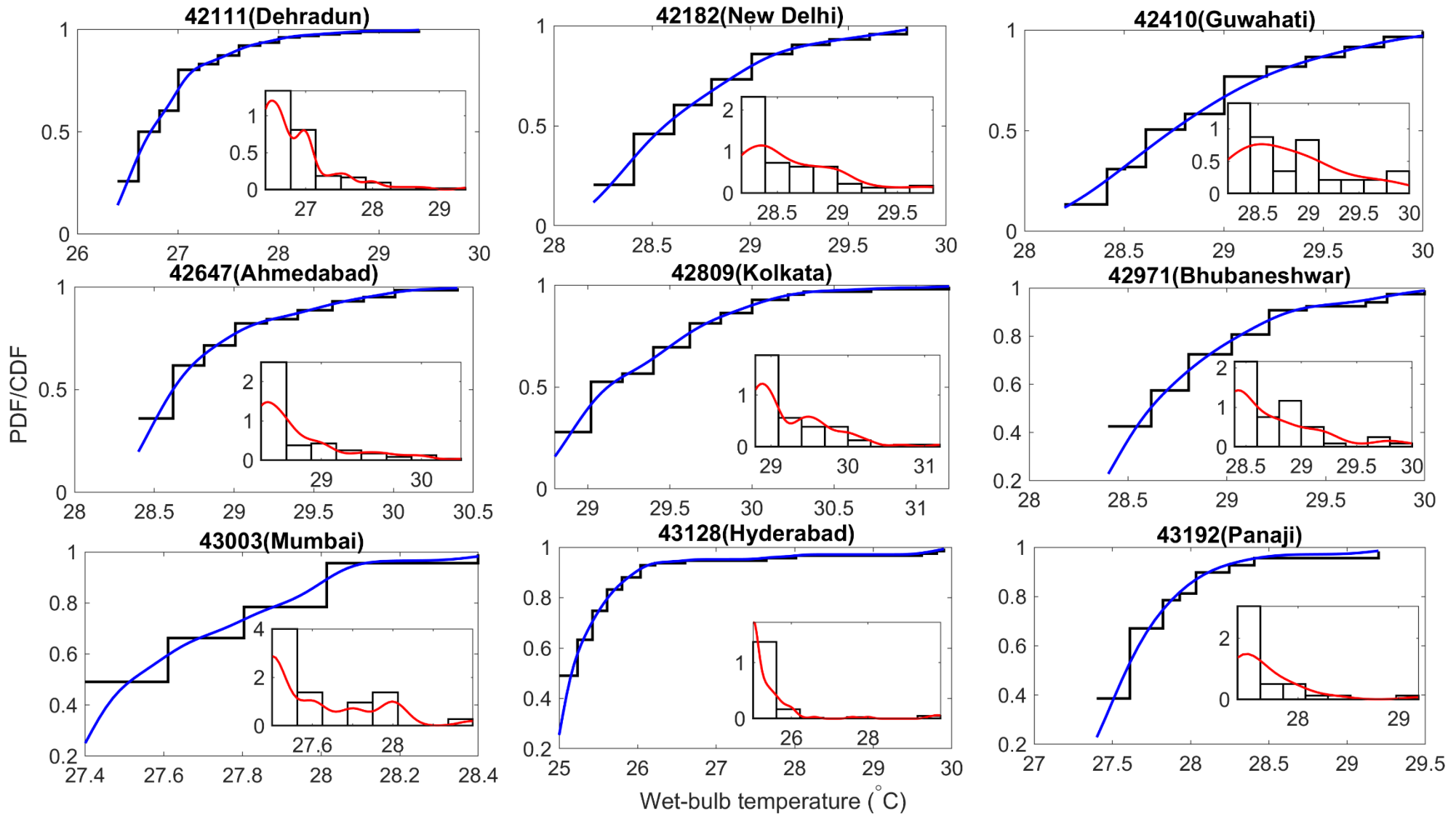


**Figure S3.** Distribution fits for WBT for Case I (POT). The inset shows the fit of probability density function. The empirical CDF is shown in solid black lines, whereas the fitted theoretical distribution is shown using blue lines.

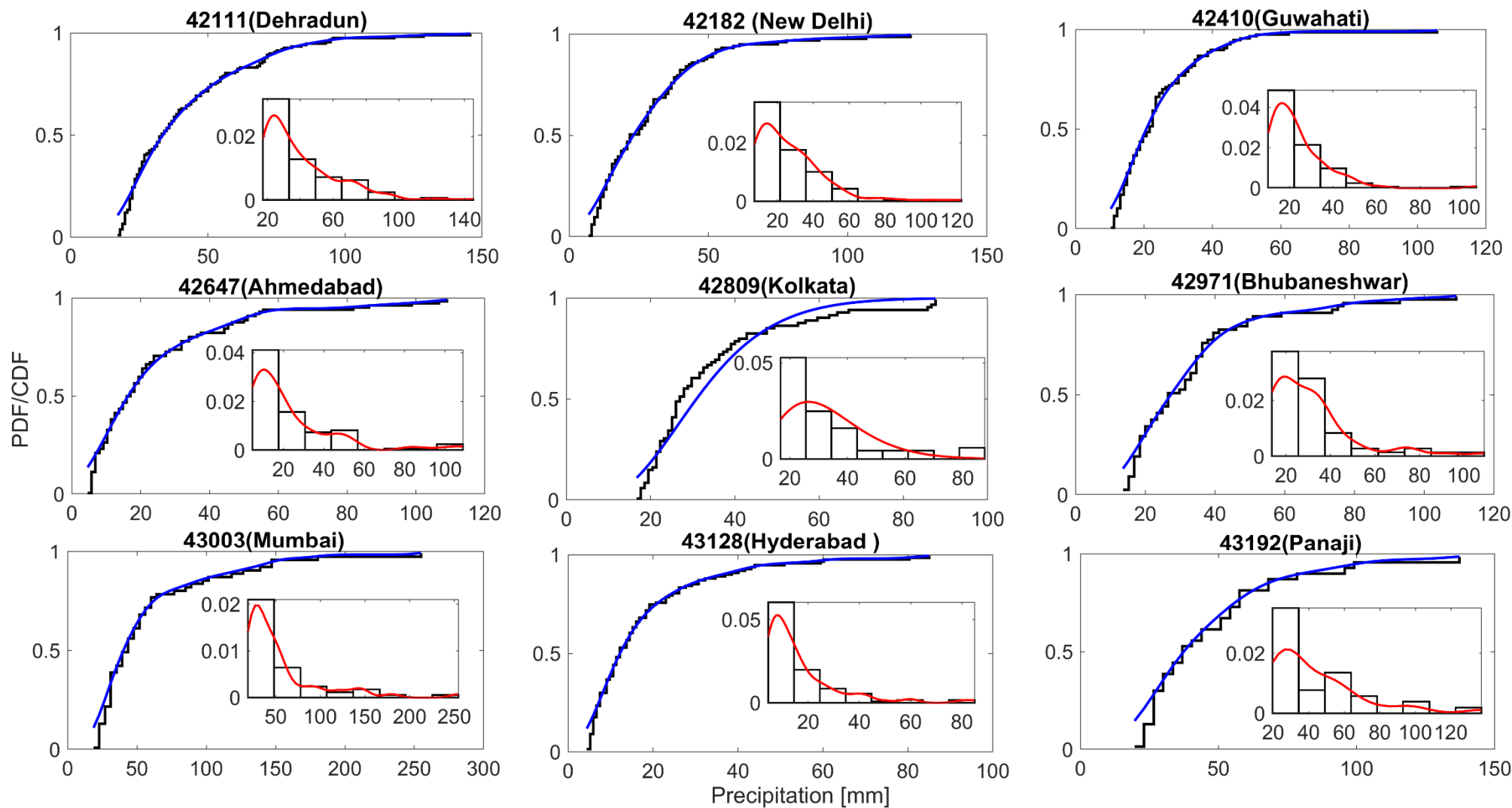


**Figure S4.** Distribution fits for precipitation for Case II (AMX). The empirical CDF is shown in solid black lines, whereas the fitted theoretical distribution is shown using blue lines.

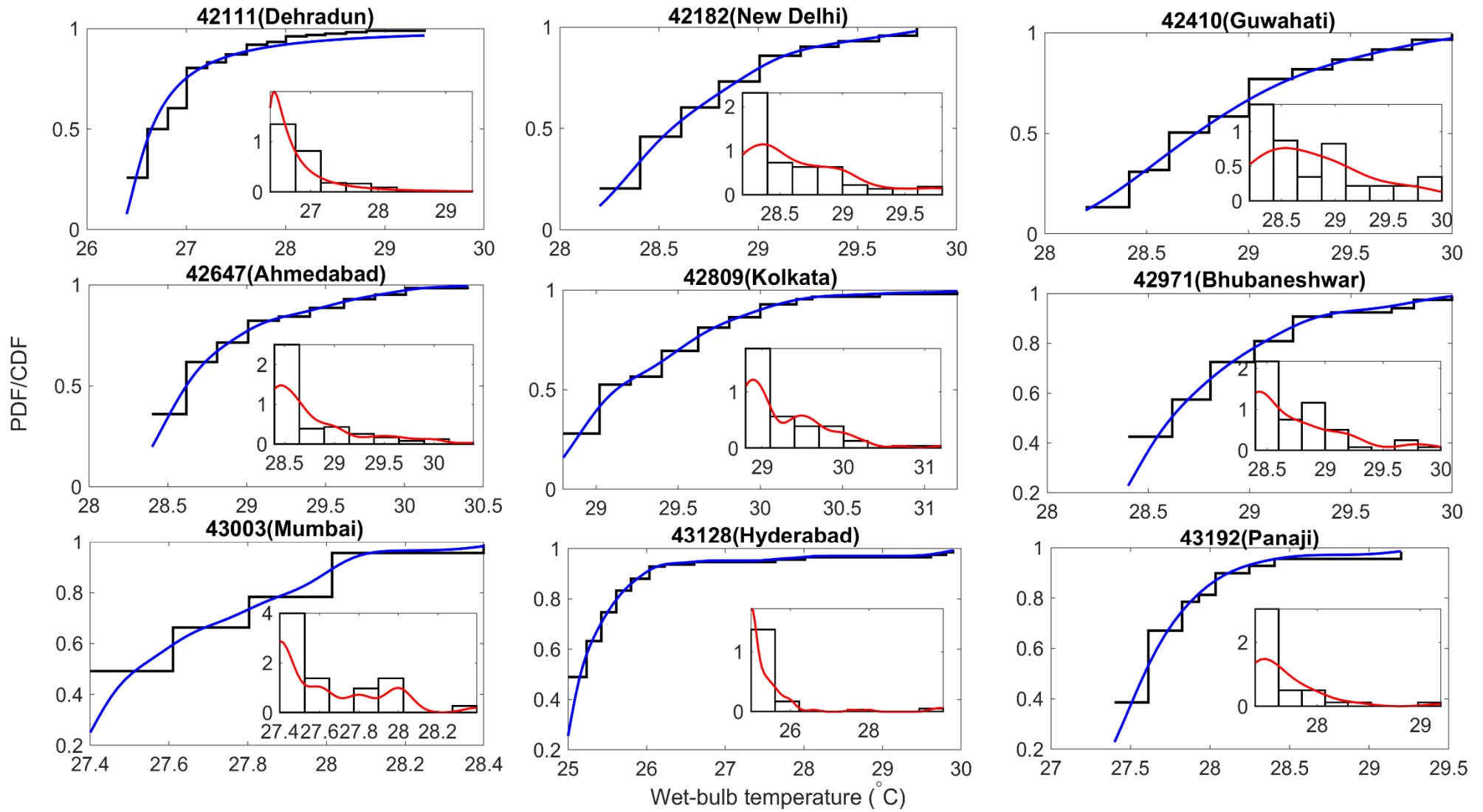


**Figure S5.** Distribution fits for WBT for Case II (AMX). The empirical CDF is shown in solid black lines, whereas the fitted theoretical distribution is shown using blue lines.

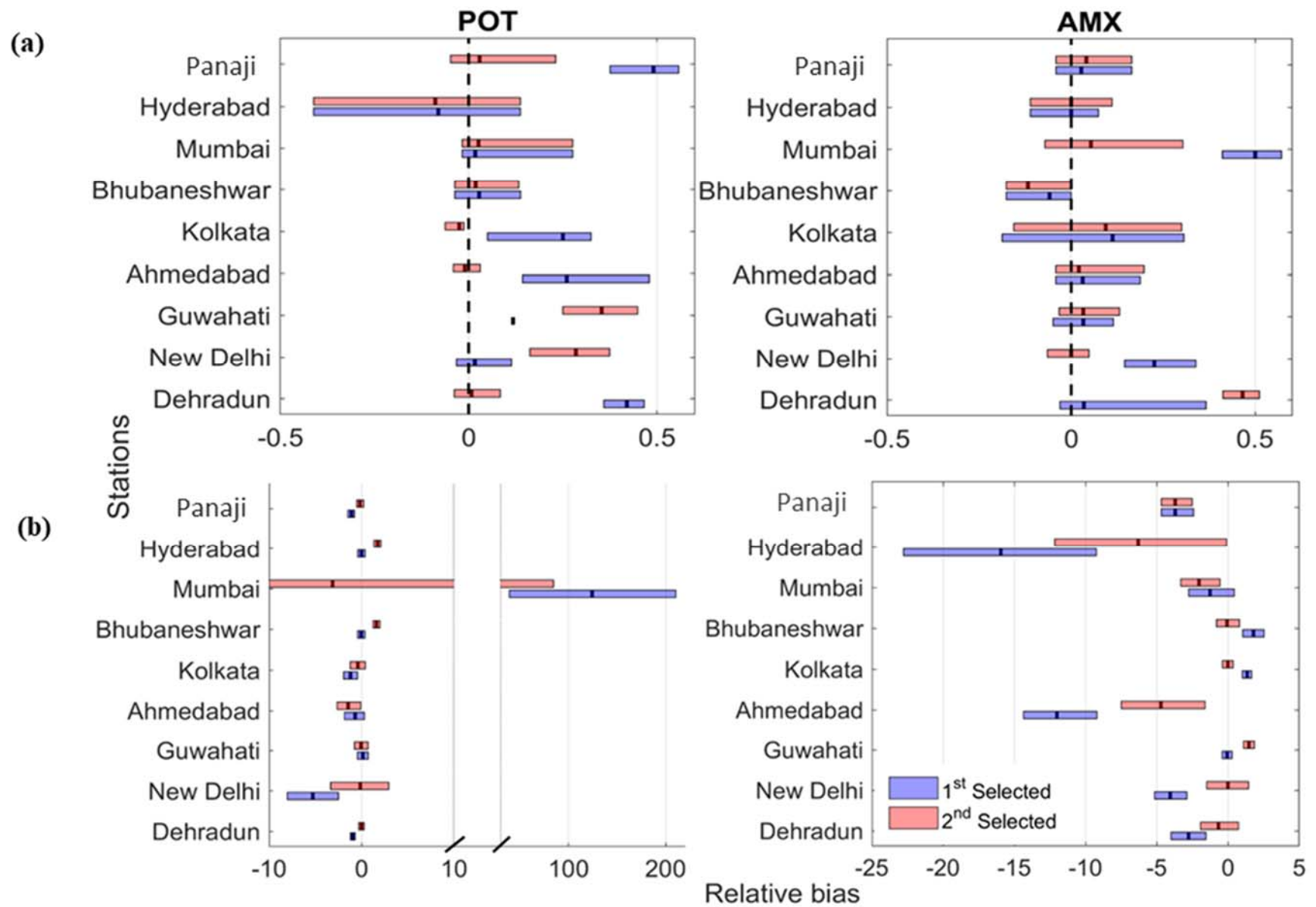


**Figure S6.** Relative bias for (a) UTR and (b) Kendall's  $\tau$  for the best-fit and next-best fit copula families identified using parametric bootstrap approach.

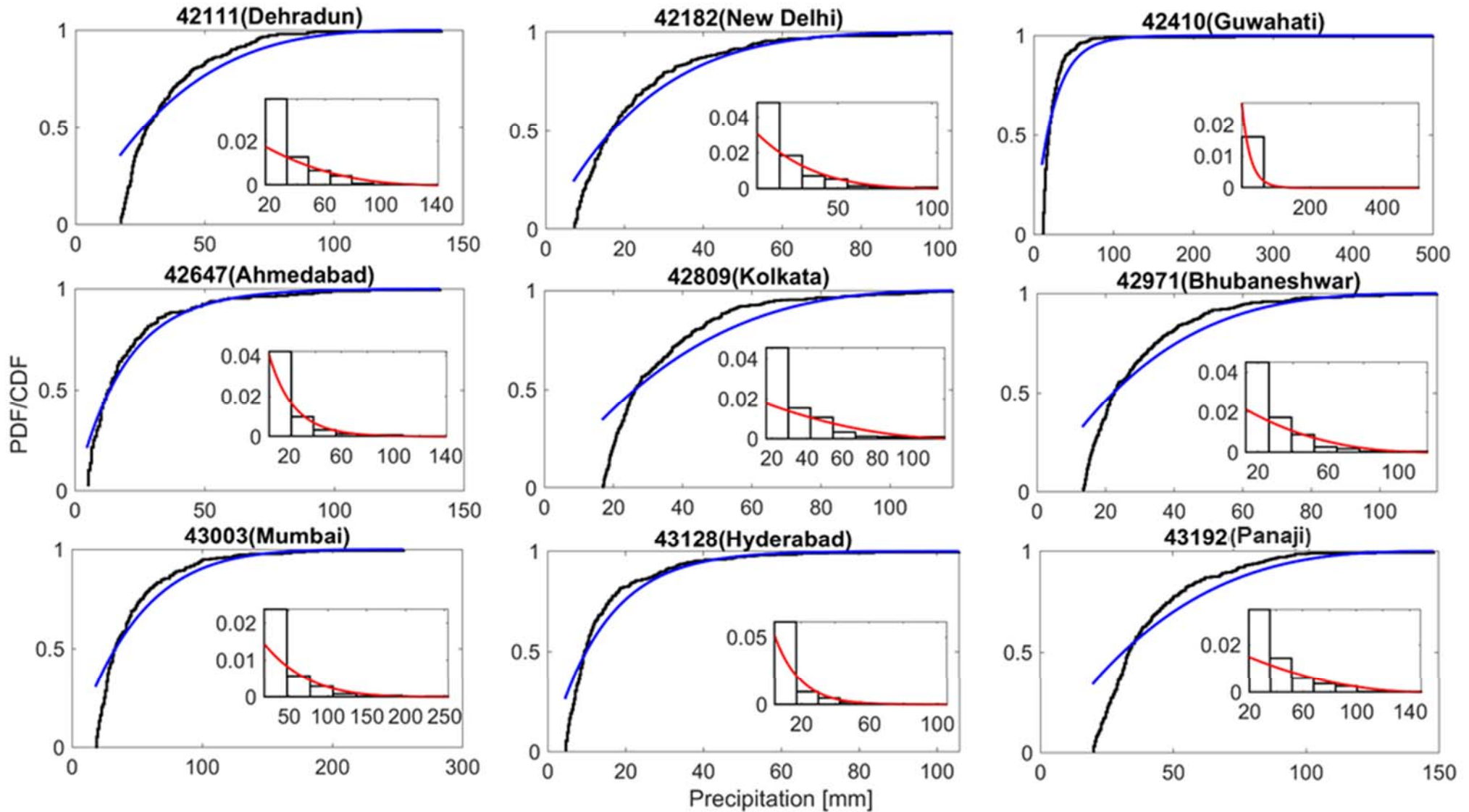


**Figure S7.** Distribution fits for Precipitation for Case I (POT) for rain-only events. The empirical CDF is shown in solid black lines, whereas the fitted theoretical distribution is shown using blue lines. The inset shows the fit of probability density function.

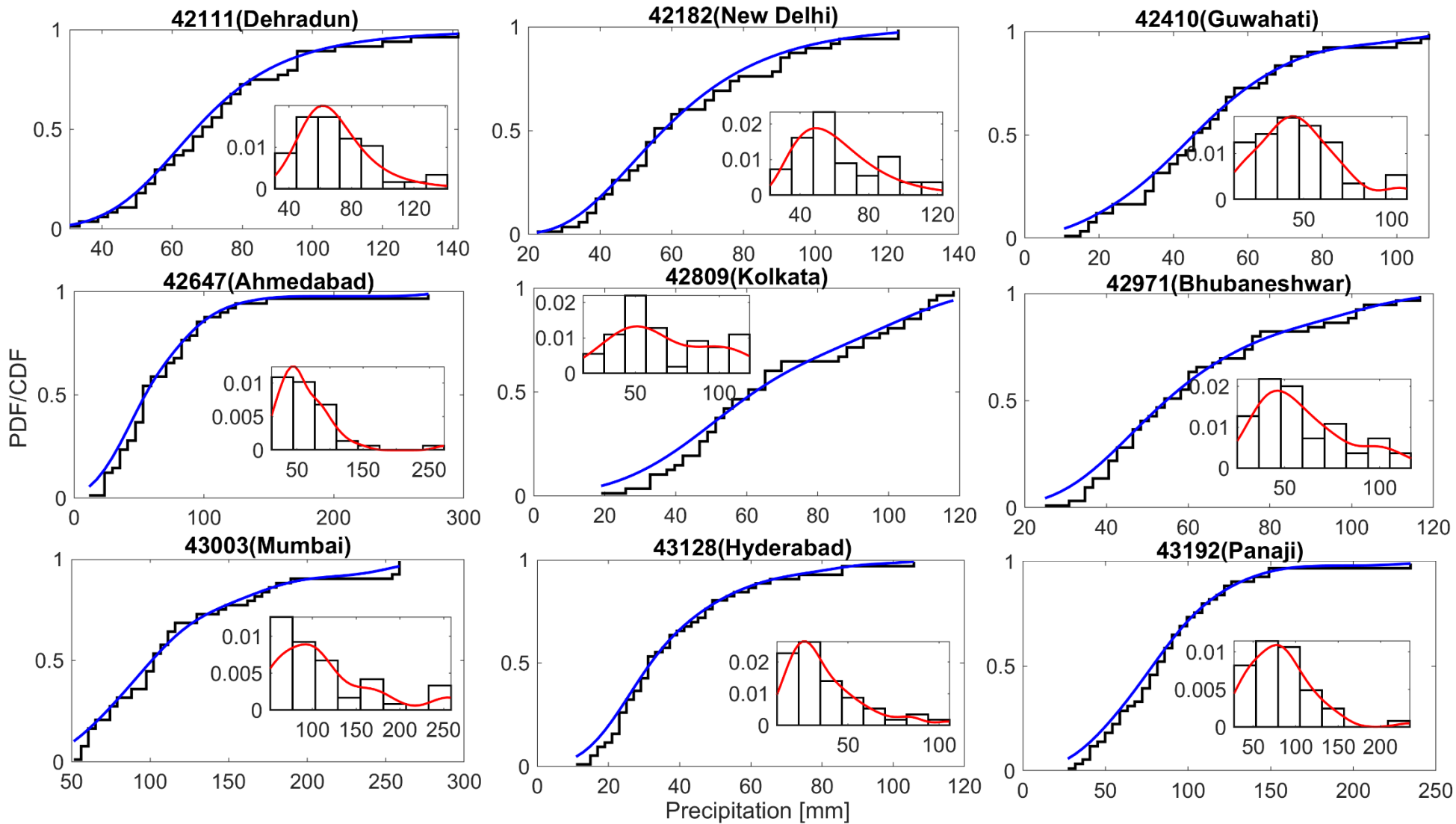


**Figure S8.** Distribution fits for Precipitation for Case II (AMX) for rain-only events. The empirical CDF is shown in solid black lines, whereas the fitted theoretical distribution is shown using blue lines.

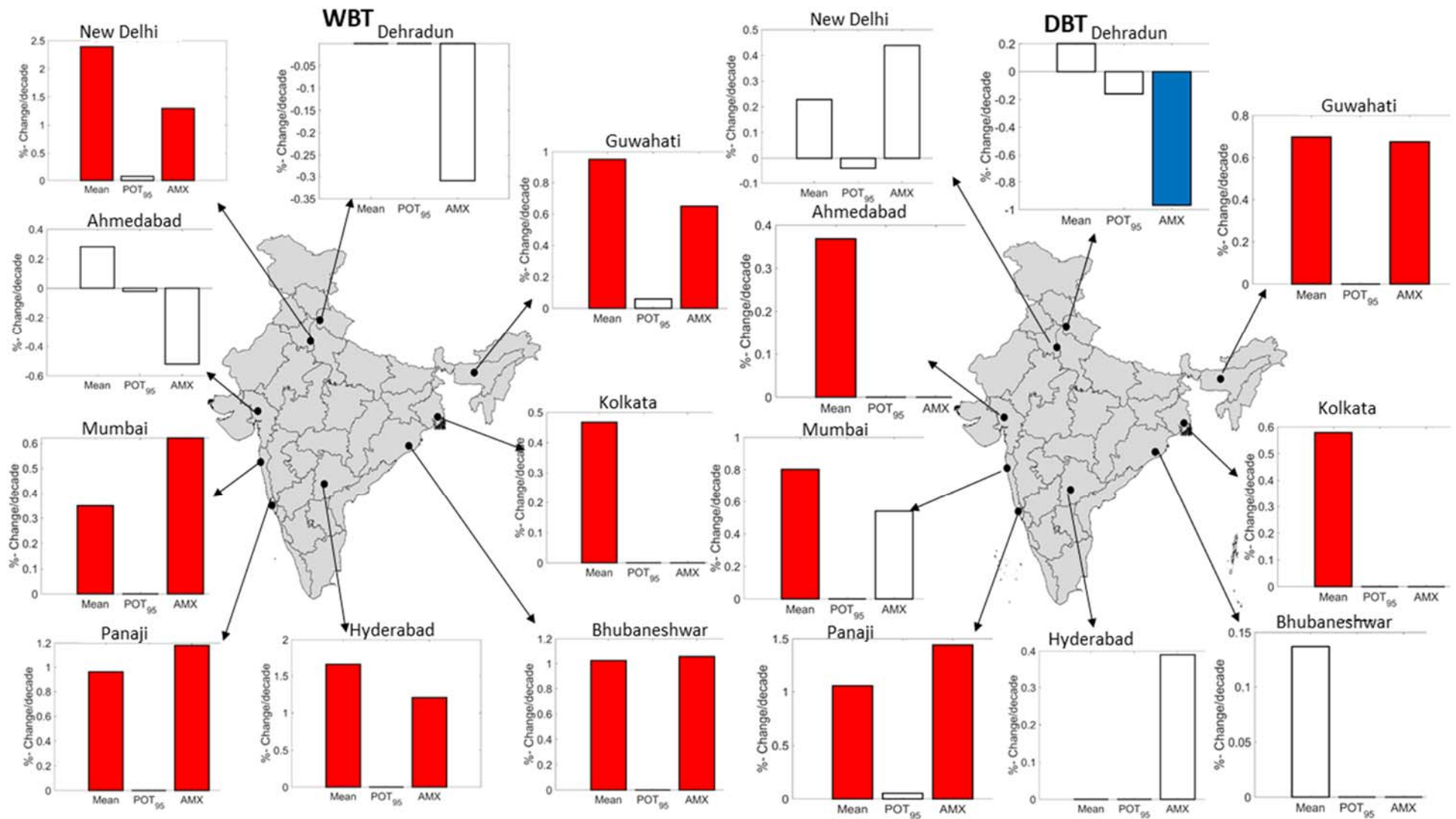


**Figure S9.** Trends in Mean and Extreme Dry- vs Wet-Bulb Temperature. Bar-plot shows the trends in Mean, POT and AMX wet-(WBT) and dry-(DBT)bulb temperature respectively. The red shades of bar show positive change/decade, whereas the blue shades of bar depict negative change, above (below) the normal level, while the normal level is indicated using the 'zero' mark on the x-axis.

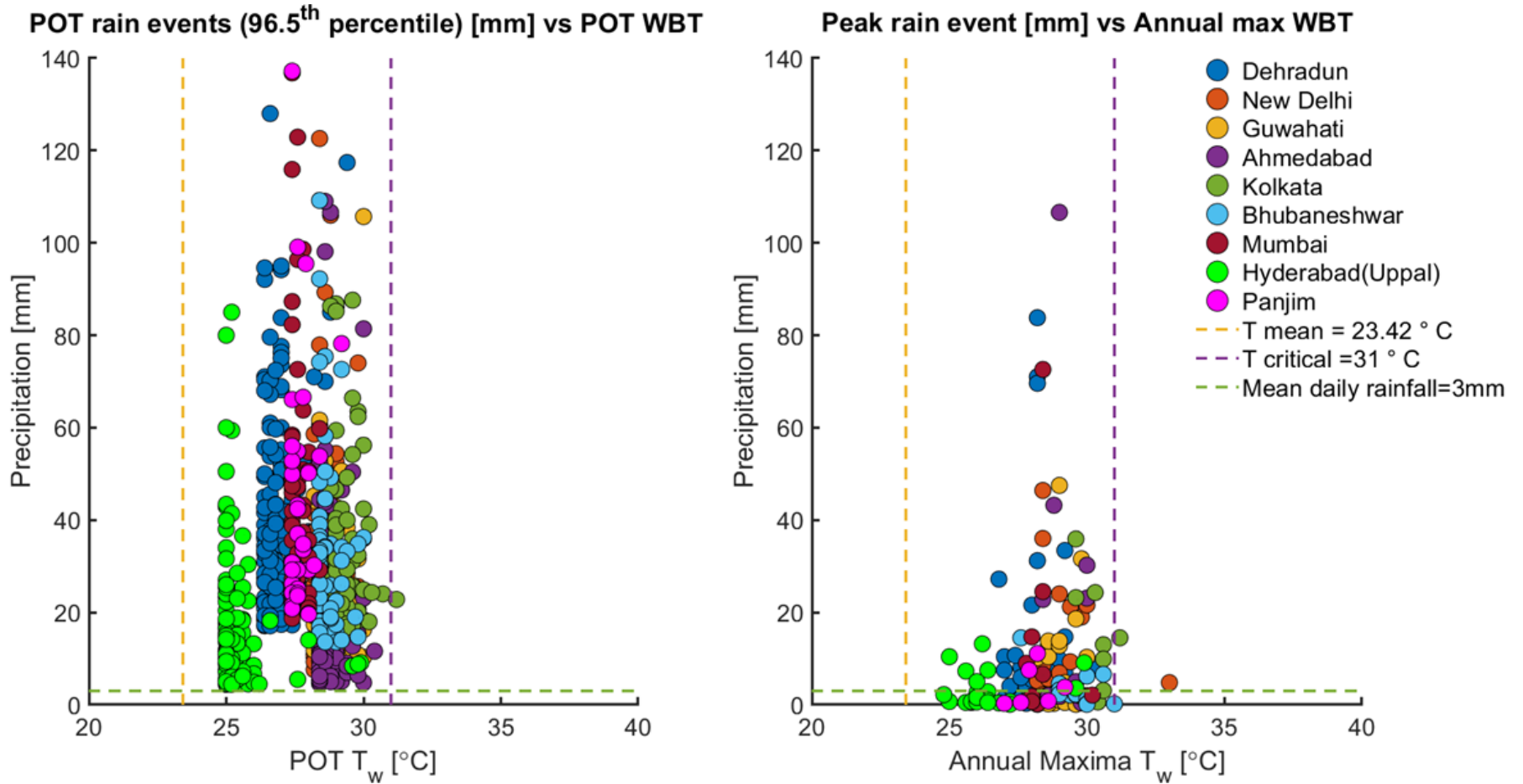


**Figure S10.** Response of peak precipitation to the extreme HSS.  $T_w$  at x-axes indicates wet-bulb temperature.  $T_w$  exceedance of 31°C, which is extremely dangerous for human (Raymond et al., 2020), is prominent for two cities, New Delhi and Kolkata. Panjim is an acronym for the city Panaji (WMO ID 43192), which is located across the western coast of peninsular India.

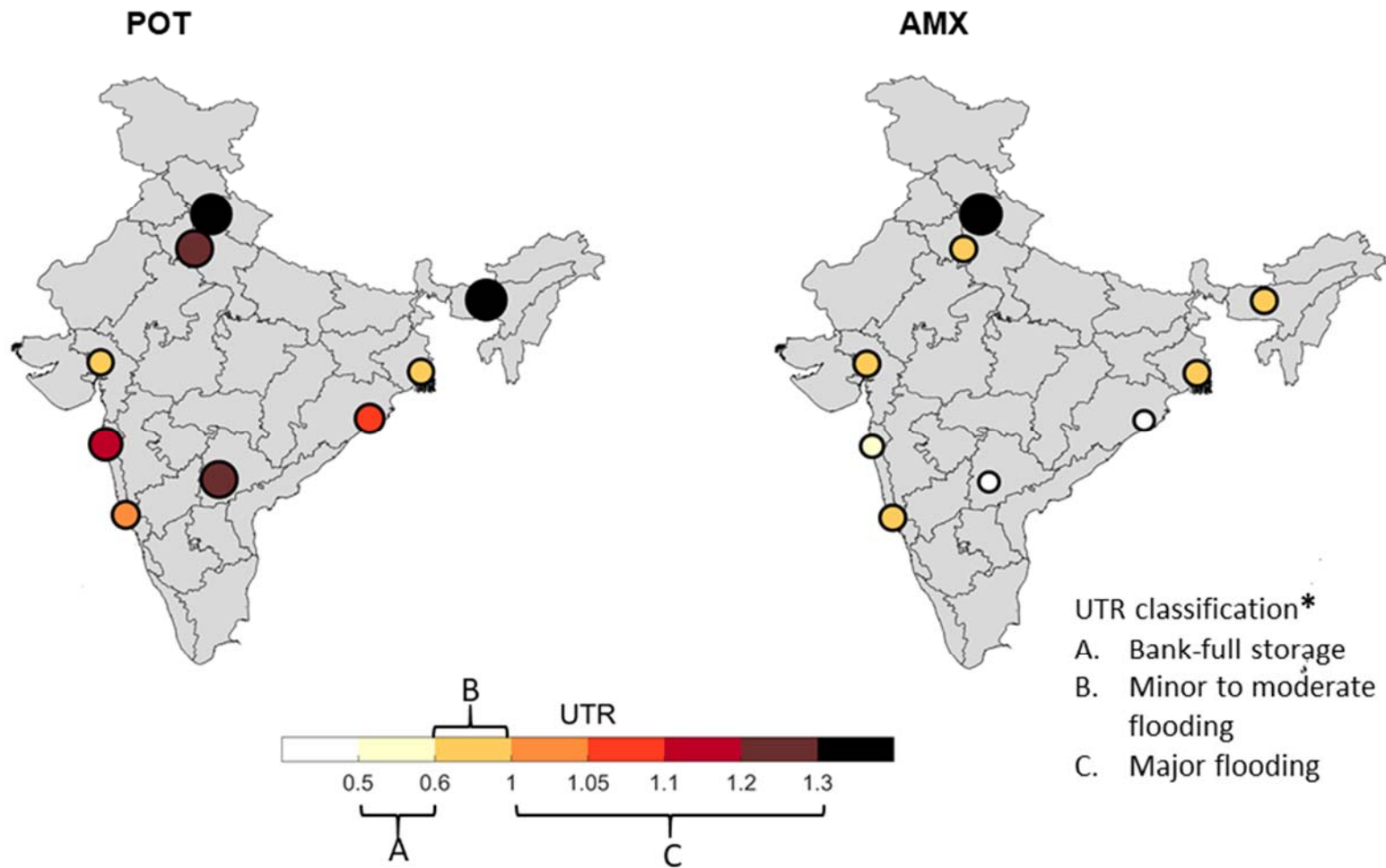


**Figure S11.** Spatial distribution of UTR (dimensionless). The size and shade of the circle is proportional to UTR magnitude. \*UTR classification is according to Villarini et al. (2014).

**Table S1.** Projected population of 2020 for selected 9 location in millions

<b>WMO ID</b>	<b>Location</b>	<b>DGR</b>	<b>Population in 2020 (in million)</b>
42111	Dehradun	0.5	0.60
42410	Guwahati	2.5	1.20
42971	Bhubaneswar	4	1.25
43003	Mumbai*	-0.3*	9.12
43128	Hyderabad	1.1	4.37
43192	Panaji	2.5	0.09
42182	New Delhi	3.4	22.04
42647	Ahmedabad	2.6	7.00
42809	Kolkata	0.1	4.54

\*  $P_{2020} = P_{2010} (1 + DGR)^N$ , where  $N = 10$ ; decadal interval considering census records at a 10-year apart, DGR denotes the decadal growth rates considering the year 2000 as baseline and was computed from percentage change in population from the year 2000 and 2010 respectively; \*shows declining DGR.

**Table S2.** Results of Marginal distribution fit and Goodness of fit statistics for POT precipitation for compound event pair Case I (POT)

Station (WMO ID)	Selected Distribution	GP		GEV		Gamma		Lognormal		Log-logistic		Kernel	
		AICc	p-value	AICc	p-value	AICc	p-value	AICc	p-value	AICc	p-value	AICc	p-value
42111	Kernel	-1151.99	0.75	-967.40	0.36	-930.74	0.07	-991.47	0.22	-981.06	0.22	<b><i>-1166.93</i></b>	0
42182	Kernel	-876.19	0.46	-774.94	0.39	-816.51	0.06	-853.42	0.48	-825.65	0.41	<b><i>-887.41</i></b>	0
42410	GP	<b><i>-838.00</i></b>	0.04	-787.03	0.56	-712.51	0.00	-775.52	0.03	-768.40	0.29	-822.95	0
42647	Kernel	-715.47	0.61	-641.06	0.44	-599.31	0.10	-679.54	0.36	-666.27	0.34	<b><i>-736.69</i></b>	0
42809	Kernel	-563.63	0.28	-592.69	0.82	-423.61	0.03	-456.35	0.04	-467.10	0.12	<b><i>-613.28</i></b>	0.05
42971	Kernel	-424.29	0.78	-395.06	0.34	-369.35	0.05	-399.21	0.23	-399.92	0.30	<b><i>-444.28</i></b>	0.01
43003	Kernel	-427.25	0.98	-428.26	0.98	-330.17	0.02	-362.98	0.12	-362.41	0.29	<b><i>-453.79</i></b>	0.02
43128	GP	<b><i>-905.87</i></b>	0.29	-787.45	0.66	-678.32	0.03	-779.42	0.28	-772.65	0.32	-882.92	0
43192	Kernel	-238.89	0.85	-217.11	0.54	-208.37	0.03	-221.55	0.19	-214.55	0.50	<b><i>-241.11</i></b>	0.02

\*The best selected distribution are based upon the minimum AIC and the graphical diagnostic plot Fig. S4. Selected distributions are marked in bold italic fonts. The abbreviations GP and GEV denote Generalized Pareto and Generalized Extreme Value distributions respectively.

**Table S3.** Results of Marginal distribution fit and Goodness of fit statistics for POT extreme WBT for compound event pair, Case I (POT)

Station (WMO ID)	Selected Distribution	GP		GEV		Gamma		Lognormal		Log-logistic		Kernel	
		AICc	p-value	AICc	p-value	AICc	p-value	AICc	p-value	AICc	p-value	AICc	p-value
42111	Kernel	-707.63	0.002	-856.00	0.016	-804.40	0	-806.70	0	-893.62	0.013	<b>-1011.34</b>	0
42182	Kernel	-501.21	0	-643.83	0.040	-606.68	0.042	-608.50	0.039	-636.54	0.137	<b>-713.23</b>	0.047
42410	Kernel	-511.72	0.006	-620.51	0.07	-578.78	0.129	-581.02	0.129	-598.77	0.166	<b>-656.09</b>	0.016
42647	Kernel	-346.89	0.001	-273.39	0	-459.84	0.019	-461.08	0.021	-505.43	0.058	<b>-606.58</b>	0
42809	Kernel	-342.73	0.002	-198.17	0.002	-427.87	0.006	-429.36	0.007	-446.88	0.07	<b>-522.13</b>	0.024
42971	Kernel	-188.44	0.002	-214.76	0.009	-295.63	0.046	-296.73	0.048	-314.28	0.072	<b>-369.53</b>	0
43003	Kernel	-154.65	0	-189.54	0.004	-260.56	0.028	-261.56	0.044	-270.80	0.088	<b>-329.43</b>	0
43128	Kernel	-416.62	0.001	-417.16	0	-487.98	0	-491.03	0	-618.21	0	<b>-729.32</b>	0
43192	Kernel	-131.19	0.009	-119.06	0.0205	-174.38	0	-174.82	0	-187.91	0.003	<b>-216.68</b>	0.002

\* For graphical diagnostic plot, see Fig. S5. Selected distributions are marked in bold italic fonts.

**Table S4.** Results of Marginal distribution fit and Goodness of fit statistics for peak precipitation event, Case II (AMX)

Station (WMO ID)	Selected Distribution	GEV		Gamma		Lognormal		Log-logistic		Kernel	
		AICc	p-value	AICc	p-value	AICc	p-value	AICc	p-value	AICc	p-value
42111	Kernel	-245.297	0.293	-230.920	0.141	-256.520	0.251	-250.160	0.422	<b>-266.846</b>	<b>0.002</b>
42182	Kernel	-202.179	0.391	-214.658	0.540	-203.771	0.450	-224.422	0.519	<b>-253.642</b>	<b>0.191</b>
42410	Kernel	-263.063	0.468	-286.326	0.709	-273.275	0.589	-278.902	0.661	<b>-301.266</b>	<b>0.227</b>
42647	Kernel	-75.003	0.813	-77.486	0.553	-81.963	0.974	-83.274	0.947	<b>-91.087</b>	<b>0.358</b>
42809	Gamma	-170.439	0.957	<b>-185.827</b>	<b>0.854</b>	-168.883	0.974	-180.638	0.874	-178.051	0.003
42971	Kernel	-143.077	0.178	-183.329	0.934	-161.883	0.470	-176.422	0.553	<b>-207.591</b>	<b>0.034</b>
43003	Kernel	-103.203	0.577	-123.737	0.583	-112.636	0.808	-115.305	0.839	<b>-128.541</b>	<b>0.002</b>
43128	Kernel	-147.465	0.263	-155.551	0.458	-136.790	0.349	-146.020	0.498	<b>-188.323</b>	<b>0.017</b>
43192	Kernel	-38.940	0.826	-45.913	0.346	-42.907	0.748	-43.141	0.811	<b>-57.817</b>	<b>0.01</b>

\* For graphical diagnostic plot, see Fig. S6. Selected distributions are marked in bold italic fonts.

**Table S5.** Results of Marginal distribution fit and Goodness of fit statistics for annual maxima WBT driver for compound event pair, Case II (AMX)

Station (WMO ID)	Selected Distribution	GEV		Gamma		Lognormal		Log-logistic		Kernel	
		AICc	p-value	AICc	p-value	AICc	p-value	AICc	p-value	AICc	p-value
42111	GEV	<b>-254.932</b>	<b>0.316</b>	-251.078	0.083	-252.618	0.087	-247.509	0.439	-252.444	0.11
42182	Kernel	-216.56	0.055	-217.566	0	-217.643	0	-230.022	0.007	<b>-248.127</b>	<b>0.251</b>
42410	Kernel	-262.29	0.166	-264.205	0.302	-265.489	0.281	-258.597	0.322	<b>-268.623</b>	<b>0.185</b>
42647	Kernel	-59.5355	0.219636	-64.1241	0.065	-64.483	0.063	-62.7834	0.221	<b>-71.3485</b>	<b>0.011</b>
42809	Kernel	-131.818	0.246	-130.656	0.177	-131.599	0.13	-130.851	0.295	<b>-146.416</b>	<b>0.03</b>
42971	Kernel	-169.781	0.076613	-172.991	0.249	-171.957	0.225	-179.503	0.451	<b>-185.521</b>	<b>0.002</b>
43003	Kernel	-103.42	0.016	-95.1025	0	-94.5348	0	-102.064	0	<b>-119.37</b>	<b>0.002</b>
43128	Kernel	-165.673	0.153	-143.523	0.047	-144.506	0.027	-147.857	0.081	<b>-184.536</b>	<b>0.402</b>
43192	Kernel	-43.7977	0.496241	-47.8339	0.452	-47.9443	0.483	-46.1709	0.301	<b>-57.8223</b>	<b>0.076</b>

\* For graphical diagnostic plot, see Fig. S7. Selected distributions are marked in bold italic fonts.

**Table S6.** Best fit and next best fit copula family based on CvM statistics for Case I (POT)

WMO ID	Location	Best fit copula				Next best fit copula			
		Copula Family	$S_{emp}$	$S_{boot}^{(k)}$	p-value	Copula Family	$S_{emp}$	$S_{boot}^C$	p-value
42111	Dehradun	AMH	0.017	0.153	1	Plackett	0.017	0.034	0.75
42182	New Delhi	Plackett	0.019	0.039	0.669	AMH	0.022	0.041	0.52
42410	Guwahati	AMH	0.023	0.047	0.628	Student's $t$	0.024	0.040	0.404
42647	Ahmedabad	AMH	0.031	0.055	0.428	Plackett	0.026	0.040	0.302
42809	Kolkata	AMH	0.037	0.078	0.644	Plackett	0.035	0.039	0.094
42971	Bhubaneswar	Student's $t$	0.032	0.041	0.197	Plackett	0.070	0.041	0.002
43003	Mumbai	Plackett	0.012	0.042	0.986	Student's $t$	0.025	0.041	0.529
43128	Hyderabad (Uppal)	Student's $t$	0.015	0.038	0.927	Plackett	0.098	0.038	0.001
43192	Panaji	AMH	0.026	0.151	0.991	Frank	0.021	0.047	0.786

**Table S7.** Best fit and next best fit copula family based on CvM statistics for Case II (AMX)

WMO ID	Location	Best fit copula				Next best fit copula			
		Copula Family	$S_{emp}$	$S_{boot}^{(k)}$	p-value	Copula Family	$S_{emp}$	$S_{boot}^C$	p-value
42111	Dehradun	Frank	0.0156	0.047	0.951	AMH	0.029	0.070	0.795
42182	New Delhi	AMH	0.033	0.124	0.947	Student's $t$	0.035	0.050	0.338
42410	Guwahati	Student's $t$	0.027	0.047	0.636	Plackette	0.043	0.045	0.067
42647	Ahmedabad	Gumbel Hougaard	0.025	0.054	0.899	Frank	0.026	0.070	0.869
42809	Kolkata	Plackette	0.022	0.054	0.831	Student's $t$	0.048	0.054	0.124
42971	Bhubaneshwar	Plackett	0.027	0.050	0.605	Student's $t$	0.044	0.052	0.145
43003	Mumbai	AMH	0.065	0.097	0.286	Frank	0.045	0.059	0.225
43128	Hyderabad (Uppal)	Frank	0.030	0.049	0.505	Plackette	0.037	0.051	0.294
43192	Panaji	Rotatory Clayton	0.013	0.045	1	Gumbel Hougaard	0.014	0.064	0.994

**Table S8.** Selected copula family based on upper tail ratio performance for Case I (POT)

Site	Mean (Best fit copula)	Mean (Next best fit copula)	Uncertainty bounds (Best fit copula)	Uncertainty bounds (Next best fit copula)	Final Selected
42111	0.420	<b>0.008</b>	0.107	<b>0.122</b>	Plackett
42182	<b>0.016</b>	0.285	<b>0.146</b>	0.211	Plackett
42410	<b>0.118</b>	0.353	<b>0.000</b>	0.199	AMH
42647	0.260	<b>0.010</b>	0.337	<b>0.071</b>	Plackett
42809	0.250	<b>0.025</b>	0.275	<b>0.050</b>	Plackett
42971	0.028	<b>0.018</b>	0.174	<b>0.170</b>	Plackett
43003	0.017	<b>0.026</b>	0.293	<b>0.293</b>	Student's t
43128	<b>0.081</b>	0.089	<b>0.548</b>	0.548	Student's t
43192	0.490	<b>0.029</b>	0.183	<b>0.279</b>	Frank

\*The font in bold indicates the selected family based on minimum central tendency as well as lower uncertainty bound. Here mean indicates the central tendency of the sample calculated using the 50<sup>th</sup> percentile or the median point. Best and next best fit copulas are selected based on Cramér–von Mises statistics. Uncertainty bound indicates Interquartile range estimated as the difference between 75<sup>th</sup> and 25<sup>th</sup> percentile of the selected sample.

**Table S9.** Selected copula family based on upper tail ratio performance for Case II (AMX)

Site	Mean (Best fit copula)	Mean (Next best fit copula)	Uncertainty bounds (Best fit copula)	Uncertainty bounds (Next best fit copula)	Final Selected
42111	<b>0.034</b>	0.466	<b>0.397</b>	0.099	Frank
42182	0.226	<b>0.000</b>	0.194	<b>0.113</b>	Student's t
42410	<b>0.033</b>	0.033	<b>0.164</b>	0.164	Student's t
42647	<b>0.031</b>	0.021	<b>0.229</b>	0.240	Gumbel Hougaard
42809	0.113	<b>0.094</b>	0.494	<b>0.456</b>	Student's t
42971	<b>0.059</b>	0.118	<b>0.176</b>	0.176	Plackett
43003	0.500	<b>0.054</b>	0.161	<b>0.375</b>	Frank
43128	<b>0.000</b>	0.000	<b>0.185</b>	0.222	Frank
43192	<b>0.027</b>	0.041	<b>0.205</b>	0.205	Rotatory Clayton

**Table S10.** Results of Marginal distribution fit and Goodness of fit statistics for POT precipitation driver for rain-only events Case I (POT)

Station (WMO ID)	Selected Distribution	GP		GEV		Gamma		Lognormal		Log-logistic		Kernel	
		AICc	p-value	AICc	p-value	AICc	p-value	AICc	p-value	AICc	p-value	AICc	p-value
42111	GP	<b>-2369.7</b>	<b>0.5</b>	-1958.7	0.2	-1810.0	0.0	-1923.2	0.1	-1944.6	0.1	-2500.2	0
42182	GP	<b>-2607.5</b>	<b>0.6</b>	-2077.5	0.3	-1860.0	0.0	-2105.2	0.2	-2097.6	0.1	-2539.5	0
42410	GP	<b>-3681.4</b>	<b>0.0</b>	-3194.2	0.3	-2657.2	0.0	-3027.8	0.0	-3106.7	0.0	-3674.5	0
42647	GP	<b>-2004.5</b>	<b>0.2</b>	-1639.0	0.3	-1475.6	0.0	-1727.5	0.2	-1735.0	0.2	-2052.3	0
42809	GP	<b>-3428.6</b>	<b>0.9</b>	-2755.8	0.1	-2414.8	0.0	-2597.5	0.1	-2659.2	0.1	-3478.0	0
42971	GP	<b>-3381.6</b>	<b>0.8</b>	-2602.2	0.2	-2336.8	0.0	-2540.1	0.1	-2588.0	0.1	-3259.5	0
43003	GP	<b>-2414.8</b>	<b>1.0</b>	-1913.1	0.3	-1629.4	0.0	-1790.7	0.1	-1818.1	0.1	-2308.6	0
43128	GP	<b>-3255.8</b>	<b>0.6</b>	-2826.8	0.4	-2213.9	0.0	-2503.5	0.1	-2561.6	0.1	-3360.8	0
43192	GP	<b>-2525.5</b>	<b>0.6</b>	-2217.4	0.3	-1839.3	0.0	-1992.7	0.1	-2030.1	0.1	-2663.5	0

\*For the graphical diagnostic plot see Fig. S7. Selected distributions are marked in bold italic fonts.

**Table S11.** Results of Marginal distribution fit and Goodness of fit statistics for peak precipitation driver for Rain-only events, Case II (AMX)

Station (WMO ID)	Selected Distribution	GEV		Gamma		Lognormal		Log-logistic		Kernel	
		AICc	p-value	AICc	p-value	AICc	p-value	AICc	p-value	AICc	p-value
42111	Log-logistic	-306.0	0.9	-303.8	0.4	-308.9	1.0	<b>-315.2</b>	<b>1.0</b>	-300.4	0.6
42182	Lognormal	-288.9	0.6	-287.3	0.5	-300.1	0.7	<b>-288.2</b>	<b>0.6</b>	-299.6	0.3
42410	Kernel	-323.1	0.4	-315.6	0.7	-286.3	0.6	-317.7	0.6	<b>-336.8</b>	<b>0.5</b>
42647	Kernel	-318.7	0.1	-315.4	0.0	-318.4	0.2	-327.4	0.6	<b>-331.1</b>	<b>0.1</b>
42809	Kernel	-242.6	0.3	-253.1	0.5	-257.0	0.4	-254.0	0.5	<b>-277.2</b>	<b>0.3</b>
42971	Kernel	-315.3	0.5	-297.9	0.3	-315.5	0.4	-304.8	0.5	<b>-333.7</b>	<b>0.2</b>
43003	Kernel	-292.3	0.5	-267.2	0.1	-284.9	0.2	-282.7	0.3	<b>-323.4</b>	<b>0.1</b>
43128	Kernel	-359.3	0.9	-317.1	0.2	-352.6	0.5	-339.2	0.7	<b>-363.6</b>	<b>0.5</b>
43192	Kernel	-342.1	0.1	-355.9	0.1	-332.7	0.3	-350.0	0.9	<b>-359.2</b>	<b>0.6</b>

\* For graphical diagnostic plot, see Fig. S8. Selected distributions are marked in bold italic fonts.

## References

- Ganguli, P., Paprotny, D., Hasan, M., Güntner, A., & Merz, B. (2020). Projected Changes in Compound Flood Hazard From Riverine and Coastal Floods in Northwestern Europe. *Earth's Future*, 8(11).  
<https://doi.org/10.1029/2020EF001752>
- O'Connor, J. E., & Costa, J. E. (2004). Spatial distribution of the largest rainfall-runoff floods from basins between 2.6 and 26,000 km<sup>2</sup> in the United States and Puerto Rico. *Water Resources Research*, 40(1).
- Rémillard, B. (2017). Goodness-of-Fit Tests for Copulas of Multivariate Time Series. *Econometrics*, 5(1), 13.
- Raymond, C., Matthews, T., & Horton, R. M. (2020). The emergence of heat and humidity too severe for human tolerance. *Science Advances*, 6(19), eaaw1838.
- Rowe, S. T., & Villarini, G. (2013). Flooding associated with predecessor rain events over the Midwest United States. *Environmental Research Letters*, 8(2), 024007.
- Soman, M. K., & Kumar, K. K. (1990). Some aspects of daily rainfall distribution over India during the southwest monsoon season. *International Journal of Climatology*, 10(3), 299–311.
- Villarini, G., & Smith, J. A. (2010). Flood peak distributions for the eastern United States. *Water Resources Research*, 46(6).
- Villarini, G., Smith, J. A., Baeck, M. L., Marchok, T., & Vecchi, G. A. (2011). Characterization of rainfall distribution and flooding associated with US landfalling tropical cyclones: Analyses of Hurricanes Frances, Ivan, and Jeanne (2004). *Journal of Geophysical Research: Atmospheres*, 116(D23).
- Villarini, G., Goska, R., Smith, J. A., & Vecchi, G. A. (2014). North Atlantic tropical cyclones and US flooding. *Bulletin of the American Meteorological Society*, 95(9), 1381–1388.
- Wietzke, L. M., Merz, B., Gerlitz, L., Kreibich, H., Guse, B., Castellarin, A., & Vorogushyn, S. (2020). Comparative analysis of scalar upper tail indicators. *Hydrological Sciences Journal*, 65(10), 1625–1639.  
<https://doi.org/10.1080/02626667.2020.1769104>